



1

2 **Regional Simulation of Indian summer Monsoon Intraseasonal Oscillations at**
3 **Gray Zone Resolution**

4

5

6

7

8

9

Xingchao Chen^{1,2,3}, Olivier M. Pauluis^{1,2}, Fuqing Zhang³

10

11

12

13

14

15

16

¹Center for Prototype Climate Modeling, New York University in Abu Dhabi, Abu Dhabi,
United Arab Emirates

17

18

19

²Courant Institute of Mathematical Sciences, New York University, New York,
New York, USA

20

21

22

23

24

25

26

27

28

Correspondence to:

29

30

31

32

33

Dr. Xingchao Chen
Email: xzc55@psu.edu



34

Abstract

35

36 Simulations of the Indian summer monsoon by cloud-permitting WRF model at gray zone
37 resolution are described in this study, with a particular emphasis on the model ability to capture
38 the Monsoon Intraseasonal Oscillations (MISO). Five boreal summers are simulated from 2007
39 to 2011 using the ERA-Interim reanalysis as lateral boundary forcing data. Our experimental
40 set-up relies on a high horizontal resolution of 9km to capture deep convection without the use of
41 a cumulus parameterization. When compared to simulations with coarser grid spacing (27-km)
42 and using the cumulus scheme, our approach results in a reduction of the biases in mean
43 precipitation and in more realistic reproduction of the low frequency variability associated with
44 MISO. Results show that the model at gray zone resolution captures the fundamental features of
45 the summer monsoon. The spatial distributions and temporal evolutions of monsoon rainfall in
46 WRF simulations are verified qualitatively well against observations from the Tropical Rainfall
47 Measurement Mission (TRMM), with regional maxima located over West Ghats, central India,
48 Himalaya foothills and the west coast of Myanmar. The onset, breaks and withdrawal of the
49 summer monsoon in each year are also realistically captured by the model. MISO phase
50 composites of monsoon rainfall, low-level wind and precipitable water anomalies in the
51 simulations are compared qualitatively with the observations. Both the simulations and
52 observations show a northeastward propagation of the MISO, with the intensification and
53 weakening of Somali Jet over the Arabian Sea during the active and break phases of the Indian
54 summer monsoon.



55 1. Introduction

56 The Indian summer monsoon (ISM) is the most vigorous weather phenomena affecting the
57 Indian subcontinent every year from June through September (JJAS). It contributes about 80% of
58 the total annual precipitation over the region (Jain and Kumar, 2012; Bollasina, 2014) and has
59 substantial influences to the agricultural and industrial productions in India. The ISM exhibits
60 strong low frequency variability in the form of “active” and “break” spells of monsoon rainfall
61 (Goswami and Ajayamohan, 2001), with two dominant modes on timescales of 30-60 days
62 (Yasunari, 1981; Sikka and Gadgil, 1980) and 10-20 days (Krishnamurti and Bhalme, 1976;
63 Chatterjee and Goswami, 2004). The low-frequency mode is generally known as the Monsoon
64 Intraseasonal Oscillation (MISO), which is closely related to the Boreal Summer Intraseasonal
65 Oscillations (BSISO, Krishnamurthy and Shukla, 2007; Suhas et al., 2013; Sabeerali et al., 2017;
66 Kikuchi et al., 2012; Lee et al., 2013) and characterized by a northeastward propagation of the
67 precipitation from the Indian Ocean to the foothills of the Himalayan foothills (Jiang et al.,
68 2004). The MISO not only affects the seasonal mean strength of the ISM, but also plays a
69 fundamental role in the interannual variability and predictability of the ISM (Goswami and
70 Ajayamohan, 2001; Ajayamohan and Goswami, 2003). The MISO phases occurring at the early
71 and late stages of the ISM also has considerable influences on the onset and withdrawal of the
72 ISM, which, in another world, determining the length of the rainy season (Sabeerali et al., 2012).
73 Hence, a more accurate forecast of the MISO assumes significance. The MISO is influenced by a
74 number of physical processes (Goswami, 1994). Its interactions with the mean monsoon
75 circulation and other tropical oscillations make its propagating characteristics more complex
76 when compared with the eastward propagating Madden Julian oscillation (MJO, Madden and
77 Julian, 1971).



78 General circulation models (GCMs) are broadly used to simulate the large-scale circulation
79 and seasonal rainfall climatology of the ISM. Results show that GCMs are able to capture the
80 fundamental features of the monsoon circulation reasonably well and also show some skills in
81 reproducing the seasonal-averaged distributions of the monsoonal rainfall (e.g., Bhaskaran et al.,
82 1995; Lau and Ploshay, 2009; Chen et al., 2011). However, the skill of the current generations of
83 GCMs in simulating and predicting the MISO remains poor (Ajayamohan et al., 2014; Lau and
84 Waliser, 2011). The computer power available nowadays constrains most GCMs to perform
85 long-term global simulations with a horizontal spacing larger than 100 km (Lucas-Picher et al.,
86 2011). As a result, the GCMs cannot well capture the high frequency atmospheric variance and
87 regional dynamics associated with the MSIO, which also leads to a systematic bias in simulating
88 the ISM rainfall (Goswami and Goswami, 2016; Srinivas et al., 2013). Increasing the spatial
89 resolution therefore is the way for GCMs (of course not the only way) to improve the MISO
90 simulation and to reduce the systematic model biases (e.g., Ramu et al., 2016; Rajendran and
91 Kitoh, 2008; Oouchi et al., 2009). However, the high resolution global simulations usually
92 require significant computational resources that most climate modeling groups cannot afford.

93 An alternative approach to improve the ISM and MISO simulations is the use of regional
94 climate models (RCMs). RCMs dynamically downscale the GCM simulations or reanalysis and
95 perform a climate simulation over a certain region of the globe (Prein et al., 2015; Giorgi, 2006).
96 Using same computer resources, RCMs are able to perform the climate simulation with much
97 higher spatial resolution and are expected to better capture the high pass atmospheric variance
98 and resolve the important regional forcings associated with topography, land-sea contrast and
99 land cover (Bhaskaran et al., 1996; Dash et al., 2006). Many previous studies found that better
100 ISM and MISO simulations can be achieved in the high resolution (typically 50km or less)



101 RCMs than that in the GCMs with coarser grid spacing (e.g., Bhaskaran et al., 1998; Kolusu et
102 al., 2014; Lucas-Picher et al., 2011; Srinivas et al., 2013; Raju et al., 2015; Samala et al., 2013;
103 Vernekar and Ji, 1999; Mukhopadhyay et al., 2010; Saeed et al., 2012). Nonetheless, apparent
104 biases of the MISO simulations can still be found in the most previous RCM studies. One
105 principle reason is, to reduce the computational requirements, the spatial resolutions used in the
106 previous RCM studies are still not high enough to resolve the convection explicitly, and
107 convective activity is represented by the cumulus parameterization schemes in the simulations.
108 However, the organization of convection is the primary mechanism for simulating the realistic
109 MISO (Ajayamohan et al., 2014). Hence, using cumulus schemes may introduce a systematic
110 bias in simulating the MISO and the monsoon rainfall climatology (Mukhopadhyay et al., 2010;
111 Das et al., 2001; Ratnam and Kumar, 2005). In addition, the cumulus parameterization schemes
112 can also interact with other parameterization schemes, such as the planetary boundary layer,
113 radiation and microphysical schemes, which may imply far-reaching consequences through
114 nonlinearities and affects the simulation of the MISO (Prein et al., 2015).

115 The alternative to the use of a convective parameterization is to rely on the internal dynamics
116 to resolve convective motion. A consensus view is that Cloud Resolving Models (CRMs) must
117 have a horizontal resolution of at least 2km to resolve the dynamics of deep convection, albeit
118 even finer resolution are necessary in order to adequately resolve the turbulent motions in
119 convective systems (Bryan et al., 2003). However, Pauluis and Garner (2006) have shown that
120 CRM with horizontal resolution as coarse as 12km can accurately reproduce the statistical
121 behavior of convection simulated at much finer resolution. This implies that a coarse resolution
122 CRM, one in which convective motion is under resolved, can nevertheless capture adequately the
123 impacts of convective motions on large scale atmospheric flows.



124 Recently, Wang et al. (2015, W15 hereafter) simulated two MJO events observed during the
125 CINDY/DYNAMO campaign using a convection-permitting regional model with 9-km grid
126 spacing. The authors compared the simulations with multiple observational datasets and found
127 that the RCM at this resolution can successfully capture the intraseasonal oscillations over the
128 tropical oceans. The horizontal grid spacing of 9 km used in W15 is not adequate for individual
129 convective cells, but enough to resolve the organized mesoscale convective systems and their
130 upscale impacts and coupling with large-scale dynamics. Hence, they called the 9-km grid
131 spacing as gray zone resolution in regional convection-permitting climate simulation. The
132 convection-permitting RCMs at the gray zone resolution have the twin advantages of (1) using
133 much less computational resources than that required by the typical cloud-resolving simulations
134 (usually, grid spacing should be smaller than 2 km) and (2) avoid using the cumulus
135 parameterization schemes. The primary objective of the present study is to evaluate the ISM and
136 MISO simulations in the RCM at the gray zone resolution, which could be an affordable and
137 efficient way for most climate model groups to achieve a cloud-permitting MISO simulation.
138 The paper is constructed as follows. Section 2 provides a brief description of the model and the
139 data used. Section 3 presents the model simulated mean ISM features and seasonal evolutions of
140 the rainfall over the monsoon region. The simulated MISO are described and compared with the
141 observations and reanalysis in section 4. Section 5 gives the concluding remarks of the study.

142

143 **2. Experimental setup and observational datasets**

144 The model configuration here is similar with the one used in W15. The Advance Research
145 WRF model (Skamarock et al., 2008), version 3.4.1, is used to simulate the ISMs over the Indian
146 subcontinent from 2007 to 2011. Simulations are performed over a single domain that covers the



147 most of South Asia with 777×444 grid points and 9-km grid spacing (Fig. 1). There are 45
148 vertical levels with a nominal top at 20 hPa and 9 levels in the lowest 1 km. Vertically
149 propagating gravity waves have been suppressed in the top 5 km of the model with the implicit
150 damping scheme (Klemp et al., 2008). The simulation employs the unified Noah land surface
151 physical scheme (Chen and Dudhia, 2001), the GCM version of the Rapid Radiative Transfer
152 Model (RRTMG) longwave radiation scheme (Iacono et al., 2008), the updated Goddard
153 shortwave scheme (Shi et al., 2010) and the WRF Double-Moment (WDM) microphysics
154 scheme (Lim and Hong, 2010) from WRF V3.5.1 with an update on the limit of the shape
155 parameters and terminal speed of snow. In W15, the authors used the Yonsei University (YSU)
156 boundary layer scheme (Hong et al., 2006) to simulate the subgrid-scale meteorological
157 processes within the planetary boundary layer. However, we find that there exists an apparent
158 dry bias in simulating the ISM precipitation after a long-term integration when YSU boundary
159 layer scheme is used. In order to improve the simulation, boundary layer scheme used for this
160 study has been changed to the new version of the asymmetric convective model (ACM2, Pleim,
161 2007). Hu et al. (2010) evaluated the different boundary schemes used in the WRF model and
162 found that ACM2 scheme can better simulate the boundary meteorological conditions of the
163 Texas region during summer than YSU scheme. Nevertheless, the sensitivity of ISM simulations
164 to the boundary-layer schemes is still deserve closer analysis and quantifications in the future,
165 which is out of the scope of the present study. Our model configuration does not use any
166 parameterization for deep convection, but rather relies on the internal dynamics to capture the
167 impact of convective activity.

168 Five boreal summers are simulated from 2007 to 2011 in this study. The 6-hourly
169 ERA-Interim reanalysis (Dee et al., 2011) is used as the initial and boundary conditions for the



170 simulations, and sea surface temperature (SST) is updated every 6 hours using the ERA-Interim
171 SST data. The model integrations start from 0000 UTC 20 April in each year. For the first 3 days,
172 a spectral nudging is applied to relax the horizontal wind with a meridional wave number 0-2 and
173 a zonal wavenumber 0-4, which constrains the large-scale flow and convergence in the domain
174 and allows the mesoscale to saturate in the spectral space (W15). The simulations are integrated
175 until October 30 for each year in order to capture the withdrawal of the ISM in different years.
176 The simulated spatial distributions and temporal variations of surface rainfall are verified against
177 the 3-hourly 0.25° TRMM 3B42 rainfall product version 7A, while the large-scale circulations
178 and atmospheric conditions in the simulations are verified against the ERA-interim reanalysis.

179 Besides the control simulations at 9 km resolution (WRF-gray hereafter), another set of
180 numerical simulations with coarser grid spacing (27km, WRF-27km hereafter) are also
181 conducted in this study to evaluate the extent to which the cloud-permitting simulations at gray
182 zone resolution can improve the simulation of the ISM and MISO. The configuration of the
183 coarse simulations is similar with WRF-gray except cumulus parameterization scheme is used to
184 represent the subgrid-scale convective activity. Mukhopadhyay et al. (2010) investigated the
185 impacts of different cumulus schemes on the systematic biases of ISM rainfall simulation in the
186 WRF RCM. They compared the simulations conducted with three different convective schemes,
187 namely the Grell–Devenyi (GD, Grell and Dévényi, 2002), the Betts–Miller–Janjić (BMJ, Janjić,
188 1994; Betts and Miller, 1986), and the Kain–Fritsch (KF, Kain, 2004) schemes. Results show
189 that KF has a high moist bias while GD shows a high dry bias in simulating the monsoonal
190 rainfall climatology. Among these three schemes, BMJ can produce the most reasonable
191 monsoonal precipitation over the Indian subcontinent with the least bias. Similar results can also



192 be found in Srinivas et al.(2013). Hence, the BMJ scheme has been used in the WRF-27km
193 simulations.

194 Fig. 2 shows the daily surface precipitation averaged over the Indian subcontinent (shown by
195 the blue polygon in Fig. 1) from TRMM observation, WRF-gray and WRF-27km during the
196 monsoon seasons (JJAS). An apparent moist bias of surface precipitation can be found for all 5
197 years (2007 to 2011) in WRF-27km, while this systematic bias is reduced considerably in
198 WRF-gray. In addition, we can find that the simulations at gray zone resolution (WRF-gray) can
199 better capture the interannual variability of the monsoon rainfall amount than the coarse WRF
200 simulations (WRF-27km). Beside the Indian subcontinent, WRF-27km also shows high moist
201 biases of surface rainfall over the adjacent oceans to the west and east coasts of India and
202 Himalaya foothills. Similar results can also be found in the earlier studies (e.g., Srinivas et al.,
203 2013). While, this moist biases over oceanic and mountainous area are reduced dramatically in
204 WRF-gray (not shown here). Results show that the monsoonal rainfall climatology can be better
205 simulated in the cloud-permitting RCM at gray zone resolution than that in the RCM using the
206 convective parameterization schemes. The rest of this paper will focus on the assessment of the
207 ISM and MISO simulations in WRF-gray while both the MISO simulations in WRF-gray and
208 WRF-27km will be compared to the observations in section 4.

209

210 **3. Mean features of Indian Summer Monsoon**

211 The large-scale atmospheric circulation and temporal-spatial patterns of the monsoon rainfall
212 in WRF-gray are first assessed in this section. Fig. 3a and 3b show the 5-yr JJAS climatological
213 mean 200-hPa winds and geopotential heights extracted from ERA-Interim and WRF-gray.
214 During the summer monsoon, the upper troposphere (200 hPa) is characterized by a strong



215 anti-cyclone over the Tibetan plateau and easterly winds over the Indian subcontinent. The
216 model well captures the wind pattern and geopotential height in the upper troposphere, though
217 the Tibetan high-pressure and easterly winds in WRF-gray are slightly stronger than that in
218 ERA-Interim (Fig. 3b). At lower level (850-hPa), the model realistically simulates the
219 geographical position and strength of Somali Jet over the Arabian Sea, with a slight
220 overestimation of the wind speed (Fig. 3c and 3d). Moisture is transported by the strong
221 low-level winds from the Arabian Sea to the Indian subcontinent. As a result, a precipitable
222 water maximum can be found over West Ghats and the Eastern coast of the Arabian Sea in both
223 in ERA-Interim and WRF-gray, though the precipitable water over the mountainous ranges of
224 West Ghats in WRF-gray is a little higher than that in ERA-Interim. In addition, WRF-gray also
225 well captures the rain shadow downwind of the mountainous areas of central and southern India
226 where a slight dry bias can be noticed (Fig. 3d). The low-level southwesterly winds over the Bay
227 of Bengal in WRF-gray are stronger than that in ERA-Interim, which leads to an overestimation
228 in the precipitable water over the north tip of the Bay of Bengal, the west coast of Myanmar and
229 the foothills of Himalaya (Fig. 3d). A comparison of JJAS-averaged daily rainfall distribution
230 observed by TRMM with that simulated by WRF-gray is shown in Figs 3e and 3f. In general,
231 WRF-gray realistically captures the spatial pattern of the monsoon rainfall with the regional
232 rainfall maximums over West Ghats, central India, Himalaya foothills and the west coast of
233 Myanmar. Consistent with the biases shown in the low-level wind and precipitable water fields
234 (Fig. 3d), the simulated surface rainfall shows a dry bias over central India and a moist bias over
235 West Ghats, Himalaya foothills and the west coast of Myanmar (the Bay of Bengal). Similar
236 features can also be found in earlier RCM studies (e.g., Lucas-Picher et al., 2011; Rockel and
237 Geyer, 2008), which have shown that these biases can be explained by the way that surface



238 schemes cannot well simulate the land-sea pressure and temperature contrasts that driving the
239 monsoon dynamics and induce an overestimation of surface wind speed over oceans. This results
240 in an overestimation of the surface evaporation over the tropical oceans and excess precipitation
241 downstream over the mountain ranges of South-East Asia.

242 The Somali Jet over the Arabian Sea is a central figure of the Indian Summer Monsoon. Its
243 emergence is crucial in determining the onset precipitation over the Indian subcontinent (Ji and
244 Vernekar, 1997; Joseph and Sijikumar, 2004). Ajayamohan (2007) proposed an index to
245 represent the Kinetic Energy (KE) of Somali Jet (KELLJ), which is defined as the mean KE of
246 winds at 850 hPa averaged over 50°-65°E and 5°-15°N (shown by the black box in Fig. 1). The
247 same index is applied here to assess the strength of Somali Jet. The 5-yr temporal evolutions of
248 KELLJ calculated from WRF-gray are compared with that calculated from ERA-Interim in Fig.
249 4. In general, the model well captures the evolution of KELLJ in different years. Sudden
250 increases in KE of Somali Jet in late May associated with the monsoon onsets are well
251 reproduced in WRF-gray. The Somali Jet is stronger during the monsoon (JJAS) than in May and
252 October, which leads to a stronger precipitation over the Indian subcontinent during the ISM.
253 WRF-gray also well simulates the intraseasonal variation of KELLJ and the decrease of KE
254 associated with the withdrawal of the monsoon in each year. Overall, the strength of Somali Jet
255 in WRF-gray is slightly stronger than that in ERA-Interim, which is similar with the above
256 analysis of Figs. 3c and 3d.

257 The evolution of surface rainfall averaged over the Indian subcontinent (shown by the blue
258 polygon) from WRF-gray is compared with that from TRMM observations (Fig. 5). Generally
259 speaking, WRF-gray well captures the mean strength and intraseasonal variation of the monsoon
260 rainfall. In these 5 years, the accumulated monsoonal rainfall amount over the Indian



261 subcontinent is largest in 2007 and smallest in 2009. 2009 is also one of the most drought years
262 in the past 3 decades. Corresponding to the evolution of Somali Jet, rainfall over the Indian
263 subcontinent begins to increase from late May, reaches its maximum during JJAS and decreases
264 again in late September or early October, which are associated with the onsets and withdrawals
265 of the ISM. The onset and withdrawal of the ISM are well captured by WRF-gray in most years
266 except the onset of the 2007 ISM in WRF-gray is later than that in TRMM observations. The
267 main reason of the 2007 ISM later onset in WRF-gray is that the super cyclonic storm Gonu
268 which induced strong precipitation over the west India and had considerable influence on the
269 onset of the 2007 ISM (Najar and Salvekar, 2010) has not been well captured in the WRF
270 simulation (the position of Gonu has a southwest shift in WRF-gray, not shown here). The ISM
271 also shows a strong ISO in each year in the form of “active” and “break” spells of monsoon
272 rainfall over the Indian subcontinent. These “active” and “break” phases of ISM are closely
273 related to the strengthening and weakening of Somali Jet (Fig. 4). Despite the biases of the
274 monsoon rainfall intensity, we can find that WRF-gray well captures most “active” and “break”
275 spells of 5-yr ISMs, which gives us confidence that the MISO can be qualitatively simulated in
276 the RCMs at gray zone resolution.

277 The spatial distributions of monthly mean precipitation from TRMM and WRF-gray in 2007,
278 2009 and 2011 are compared in Figs 6, 7 and 8. Similar with the analysis of Fig.3, the model
279 well captures the rainfall centers over West Ghats, central Indian, Himalaya foothills and the
280 west coast of Myanmar during the summer monsoon seasons, with an overestimation of
281 precipitation over the west coast of Myanmar and Himalaya foothills due to the overprediction of
282 low-level wind over the Bay of Bangle. With high spatial resolution, WRF-gray is able to
283 capture the finer details of orographic precipitation over the mountainous ranges (for example,



284 along the west coastline of the Indian subcontinent). In addition, the interannual variability of
285 monsoon rainfall is also well simulated in WRF-gray (Figs. 6, 7 and 8). In 2007, rainfall is very
286 weak over the Indian subcontinent in May though orographic precipitation can still be found over
287 the mountainous ranges along the west coastline (Figs. 6a and 6g). Accompany with the onset of
288 the ISM and the enhancement of low-level winds over the Arabian Sea, precipitation over the
289 west coast of Indian subcontinent and its adjacent oceans increases dramatically in June (Figs. 6b
290 and 6h). In July, the precipitation center along the west coast of Indian subcontinent is still
291 apparent and the precipitation over central India is increased considerably (Figs. 6c and 6i).
292 Rainfall over Himalaya foothills and the west coast of Myanmar also reaches its strongest stage
293 in this month. In August, rainfall over central India and the west coast of Myanmar are still
294 strong while the precipitation near the Himalaya foothills is decreased (Figs. 6d and 6j). The
295 rainfall intensity over the entire monsoon region decreases continually in September (Figs. 6e
296 and 6k) and the precipitation over the Indian subcontinent becomes very weak in October (Figs.
297 6f and 6l), which represents the end of the monsoon season. When compared to 2007, the ISM in
298 2009 is dryer, especially over the Indian subcontinent (Fig. 7). The onset and withdrawal of the
299 2009 ISM over the Indian subcontinent are in June and September. The significant “break” spells
300 of the 2009 ISM in June, August and September are well captured by WRF-gray (Figs. 5c, 7h, 7j
301 and 7k). The evolution of monthly mean precipitation in 2011 (Fig. 8) is similar with that in
302 2007 (Fig. 6) with the rainfall over the central India reaches its strongest stage in August (Figs.
303 8d and 8j). In May 2011, an apparent moist bias of precipitation can be found over the Arabian
304 Sea in WRF-gray, which is induced by the formation of an unreal tropical cyclone in the
305 simulation. Generally speaking, WRF-gray is able to capture the spatial and temporal features of
306 the ISM rainfall. Though apparent biases can still be found, the intensity and spatial pattern of



307 monsoon rainfall in WRF-gray are verified well against the observations, especially over the
308 Indian subcontinent.

309

310 **4. Monsoon Intraseasonal Oscillations (MISO)**

311 As mentioned in the Introduction, the MISO has fundamental influences on the seasonal
312 mean, predictability and interannual variability of the ISM. Hence, the simulation of the MISO is
313 very important for the credibility of the model in simulating the ISM. The section evaluates the
314 ability of WRF-gray in simulating the MISO. MISO Phase composites of the surface rainfall and
315 large-scale flows from WRF-gray are compared with that from the observations

316

317 **4.1 Indices for the MISO**

318 Using the developed nonlinear Laplacian spectral analysis (NLSA) technique (Giannakis and
319 Majda, 2012a, b), Sabeerali et al. (2017) developed improved indices for real-time monitoring of
320 the MISO. Compared to the classical covariance-based approaches (for example Suhas et al.,
321 2013), a key advantage of NLSA is that it is able to extract the spatiotemporal modes of
322 variability spanning multiple timescales without requiring bandpass filtering or seasonal
323 partitioning of the input data. The MISO indices constructed by NLSA better resolve the
324 temporal and spatial characteristics of the MISO when compared to the conventional
325 EEOF-based MISO indices. In order to evaluate the MISO simulation in WRF-gray, the NLSA
326 MISO indices are applied in this study to construct the phase composites of rainfall and
327 atmospheric circulation from WRF-gray and the observations. Fig. 9 shows the daily evolution
328 of the MISO in each year monitored by the two-dimensional phase space diagram constructed
329 from the NLSA MISO indices. As with Sabeerali et al. (2017), all indices are extracted from the



330 daily GPCP rainfall dataset (Huffman et al., 2001). The 2D phase space of the NLSA MISO
331 indices is divided into 8 phases to represent different phases of the MISO. The significant MISO
332 event is defined as the instantaneous MISO whose amplitude is greater than 1.5 (shown by the
333 black circle in Fig. 9). From Fig. 9, we can find that the MISO activity in 2007, 2008 and 2009
334 are much more significant than that in 2010 and 2011. Among these five years, the accumulated
335 monsoon rainfall amount over the Indian subcontinent is highest in 2007, which also features the
336 strongest MISO activity (Fig. 9a). The following year, 2008, is also a moist year with strong
337 MISO activity is from mid-June to the end of September (Fig. 9b). In 2009 (Fig. 9c), a severe
338 drought year, the MISO is weak during the early and late stages of the monsoon season (June and
339 September), but stronger in the midst of the monsoon season (July and August). The amplitude
340 of the MISO indices in 2010 and 2011 are much smaller, while significant MISO events can still
341 be found in September 2010 (Fig. 9d) and most monsoon months in 2011 (Fig. 9e).

342

343 **4.2 Phase composites of surface rainfall**

344 Fig. 10 shows the phase composites of daily surface rainfall anomalies (subtracted the mean
345 daily rainfall of 5-yr monsoon seasons) obtained from TRMM observation based on the NLSA
346 MISO indices. The phase composites are computed by averaging the significant MISO activities
347 in each phase space occurred in the 5-yr monsoon seasons. An apparent northeastward
348 propagation of the MISO can be found in the phase composites (from the phase 1 to the phase 8),
349 which corresponds to the anticlockwise rotation in the 2D phase space of the MISO indices (Fig.
350 9). Phase 1 shows the formation of enhanced rainfall anomalies over the tropic Indian Ocean (Fig.
351 10a). During this Phase, rainfall over the Indian subcontinent is suppressed. The enhanced
352 rainfall anomalies over the tropic ocean become stronger and move toward the Indian



353 subcontinent in Phase 2 (Fig. 10b) and reach West Ghats and its adjoining oceans in Phase 3 (Fig.
354 10c). In Phase 3, precipitation over the Indian subcontinent is enhanced while rainfall over the
355 Bay of Bengal is suppressed (Fig. 10c). Rainfall over central India and the south part of the Bay
356 of Bengal are enhanced considerably in Phase 4 (Fig. 10d) and form into a northwest-southeast
357 enhanced rainfall line that stretches from the west coast of the Indian subcontinent to the south of
358 the Indochina in Phase 5 (Fig. 10e). This enhanced rainfall line continually propagates to
359 northeast in Phase 6 (Fig. 10f) and collapses in Phase 7 (Fig. 10g). In Phase 7, the enhanced
360 rainfall anomalies can still be found over north India while the rainfall in south India is
361 suppressed by the MISO. The total rainfall over the entire basin is weakest during Phase 8 with
362 the rainfall anomalies are mostly negative over the inland regions of India (Fig. 10h). However,
363 rainfall near Himalaya foothills begins to increase in this phase and reaches its maximum in
364 Phase 2 (Fig. 10b). The phase composites of daily surface rainfall anomalies obtained from 5-yr
365 TRMM observations in this study are similar to the 26-yr phase composites in Sabeerali et al.
366 (2017), which shows that the 5-yr rainfall statistic reflects the climatological characteristics of
367 the MISO.

368 Fig.11 presents the phase composites of daily surface rainfall anomalies obtained from
369 WRF-gray. Despite differences in the intensity and location of rainfall anomalies, the MISO
370 simulation in WRF-gray verified well against the TRMM observations. The fundamental features
371 of rainfall anomalies in all 8 Phases of the MISO are well captured by WRF-gray: for example,
372 the northeastward propagation of the enhanced rainfall anomalies, the “active” and “break”
373 phases of the monsoon rainfall over the Indian subcontinent, the northwest-southeast enhanced
374 rainfall line in Phases 5 and 6, the increase of rainfall over Himalaya foothills from Phase 8 to
375 Phase 2 and so on. Nonetheless, we should also notice that the amplitude of the rainfall



376 anomalies in WRF-gray is slightly larger than that in the TRMM observations, which reflects
377 that the model simulated MISO is stronger than the real one in the satellite observations.

378 In order to evaluate to what extent the RCM at gray zone resolution can improve the
379 simulation of the MISO, the phase composites of daily surface rainfall anomalies obtained from
380 WRF-27km (Fig. 12) are also compared with that from the TRMM observations (Fig. 10) and
381 WRF-gray (Fig. 11) in this section. We can find that the amplitude of rainfall anomalies in
382 WRF-27km is much larger than that in WRF-gray and TRMM observations, which shows the
383 WRF-27km has larger systematic biases than WRF-gray in simulating the MISO intensity.
384 Though WRF-27km can also basically capture the “active” (Figs 12c, 12d, 12e and 12f) and
385 “break” (Figs. 12g, 12h, 12a and 12b) phases of the ISM, it shows a larger bias in the
386 spatial-temporal distributions of the rainfall anomalies during the different phases of the MISO
387 than WRF-gray. For example, the rainfall anomalies in Phase 1, 2 and 3 (Figs. 12a, 12b and 12c)
388 are shifted northward, consistent with a faster development of the MISO cycle in the coarse
389 resolution model. The northwest-southeast enhanced rainfall line shown in TRMM observations
390 and WRF-gray is not clear in WRF-27km. This could be possibly due to deficiencies in how
391 WRF-27km capture stratiform rainfall, which would create a bias toward more patchy, deep
392 convective events. The increase of rainfall over Himalaya foothills from Phase 8 to Phase 2 has
393 not been well simulated in WRF-27km. Generally speaking, WRF-gray better simulates the
394 MISO than WRF-27km, both in the aspects of intensity and the spatial-temporal evolution.

395 Besides the phase composite, the evolutions of 10-day averaged daily surface rainfall
396 anomalies in WRF-gray and TRMM observations are also compared with each other to further
397 access the credibility of WRF-gray in simulating the intraseasonal variability of the ISM. 10-day
398 evolutions of rainfall anomalies from 1 July to 10 August, 2009 in TRMM observations and



399 WRF-gray are shown in Fig. 13. During this period, the monsoon rainfall over the Indian
400 subcontinent turns from a strong “active” phase to a strong “break” phase (Fig. 5c). The rainfall
401 is enhanced over the west coast of the Indian subcontinent, central India and the Bay of Bengal
402 in the first ten days of July (Fig. 7a), which is similar with the combined features of Phases 3 and
403 4 (Figs. 10c and 10d). The enhanced rainfall anomalies form into a northwest-southeast line in
404 the middle of July (Fig. 7b), which corresponds to Phases 5 and 6. In the end of July, rainfall
405 over most area of the Indian subcontinent is suppressed while the rainfall anomalies over north
406 India is still positive (Fig. 7c). In early August, rainfall anomalies over the entire Indian
407 subcontinent turn to negative with rainfall over Himalaya foothills is enhanced (Fig. 7d), which
408 is similar to the combined features of Phases 8, 1 and 2 (Figs. 10h, 10a and 10b). Though small
409 biases can be found in the simulated rainfall intensity and location, the 10-day evolutions of daily
410 rainfall anomalies in WRF-gray verified well against the TRMM observations (Figs. 13e-h),
411 which again proves that the cloud-permitting RCM at gray zone resolution is credible in
412 simulating the MISO.

413

414 **4.3 Phase composites of atmospheric circulation**

415 During the different phases of the MISO, the large-scale flows and atmospheric conditions
416 also exhibit different behaviors (Raju et al., 2015; Goswami et al., 2003; Mukhopadhyay et al.,
417 2010). Fig. 14 shows the phase composites of 850-hPa wind and precipitable water anomalies
418 obtained from ERA-Interim. Consistent with the phase evolution of the enhanced daily rainfall
419 anomalies (Fig. 10), the precipitable water anomalies also show an apparent northeastward
420 propagation from Phase 1 (Fig. 14a) to Phase 8 (Fig. 14h), which corresponds to the
421 anticlockwise rotation in the 2D phase space of the MISO indices (Fig. 9). The major features of



422 the MISO active phase (Fig. 14e) are the formation of low pressure anomalies over northwest
423 and central India which is associated with the southward shifting of monsoon trough (Raju et al.,
424 2015). As a result, the strong westerly wind over the Arabian Sea and the Bay of Bengal also
425 enhanced dramatically during the active phase of the MISO, which transports more water vapor
426 from the oceans to the inland regions and leads to enhanced precipitable water anomalies over
427 the land. The strength of Somali Jet is also enhanced during the MISO active phase (Fig. 14e).
428 During the break phase of the MISO, on the other hand, high pressure anomalies can be found
429 over northwest and central India, which is associated with the northward shifting of monsoon
430 trough. The westerly wind over the Arabian Sea and Somali Jet are weakened during the break
431 phase (Figs. 14a and 14b), which lead to negative precipitation water and surface rainfall
432 anomalies over the Indian subcontinent. Fig. 15 shows the phase composites of 850-hPa wind
433 anomalies and precipitable water anomalies obtained from WRF-gray. We can find that
434 WRF-gray well produces the features of large-scale flow and precipitable water anomalies in
435 different phases of the MISO (Fig. 15), which shows that the cloud-permitting RCM at gray zone
436 resolution can also well capture the large-scale circulation features of the MISO. We should
437 notice that, as the rainfall anomalies shown in Fig. 11, the amplitudes of low-level wind and
438 precipitable water anomalies in WRF-gray (Fig. 15) are larger than that in ERA-Interim (Fig. 14),
439 which implies that the simulated MISO in WRF-gray is stronger than the real one.

440

441 **4.4 Sensitivity to initial dates**

442 While WRF-gray captures many aspects of the ISM and MISO qualitatively, quantitative
443 model biases are still apparent. These biases may be induced by various reasons such as the
444 choices of surface scheme which may induce biases in simulating the surface temperature and



445 land-sea contrast, the model domain size which have significant effects on the simulation of
446 regional features and the initial conditions which the dynamical systems may be highly sensitive
447 to. The sensitivity of WRF-gray simulation to initial dates is further investigated in this section.
448 Fig. 16 shows the temporal evolutions of Somali Jet Strength (Fig. 16a), precipitation water (Fig.
449 16b) and precipitation (Fig. 16c) averaged over the Indian subcontinent in the WRF simulations
450 at gray zone resolution started from three different days (WRF0420: blue lines, started from
451 0000 UTC 20 April; WRF0419: red lines, started from 0000 UTC 19 April; WRF0421: green
452 lines, started from 0000 UTC 21 April) in 2007. Though all three WRF simulations are forced by
453 the same lateral boundary conditions and the initial times are also close to each other, we can still
454 find apparent differences of the simulated monsoon atmospheric circulation (Fig. 16a), humidity
455 (Fig. 16b) and precipitation (Fig. 16c) in three experiments. In particular, in May, there exist
456 apparent rainfall biases in WRF0419. However the onset of the ISM is better captured by
457 WRF0419 than WRF0420 and WRF0421. The overprediction of monsoon rainfall from 15
458 September to 01 October in WRF0420 is considerably reduced in WRF0419 and WRF0421.
459 Results show that the ISM and MISO simulations in RCM at gray zone resolution are sensitive to
460 the initial conditions.

461

462 **5. Summary and discussion**

463 Simulations of the ISM by cloud-permitting WRF model at gray resolution (9 km) are
464 evaluated in this study, with a particular emphasis on the credibility of the MISO simulation. The
465 model is forced by ERA-Interim reanalysis for every year from 20 April to 30 October during
466 2007-2011. Model domain covers the entire Indian monsoon region which allows the systematic
467 evolution of the ISM internal dynamics. Compared with the RCM at coarse resolution and using



468 the cumulus parameterization scheme (WRF-27km), the systematic biases of monsoon rainfall
469 climatology in the cloud-permitting RCM at gray zone resolution (WRF-gray) are reduced
470 considerably. The interannual variability of the accumulated monsoon rainfall over the Indian
471 subcontinent is also better captured in WRF-gray.

472 Results from WRF-gray are compared quantitatively with the reanalysis and long-term TRMM
473 observations. In general, WRF-gray could reproduce the fundamental features of ISM reasonably
474 well. The Tibetan high-pressure and easterly winds at 200 hPa in WRF-gray are slightly stronger
475 than that in ERA-Interim. The low-level southwesterly winds over the Bay of Bengal in
476 WRF-gray is also stronger when compared to that in the reanalysis, which leads to an
477 overprediction of precipitable water and surface rainfall over the west coast of Myanmar and
478 Himalaya foothills in WRF-gray. The temporal evolutions of Somali jet and surface rainfall
479 averaged over the Indian subcontinent are also well simulated in WRF-gray. The model captures
480 most onsets, breaks and withdrawals of the ISMs, while the ISM onset in 2007 is later in
481 WRF-gray than that in TRMM observation. Spatial distributions of monthly mean precipitation
482 from TRMM and WRF-gray are further compared in the current study. Results show that
483 WRF-gray could reproduce the spatial patterns of the monthly rainfall in each year and well
484 capture the monsoon rainfall centers over West Ghats, central India, Himalaya foothills and the
485 west coast of Myanmar. However, biases of rainfall intensity and position can still be found in
486 WRF-gray, for example, the model simulates an unreal tropical cyclone over the Arabian Sea in
487 May 2011.

488 Because the MISO has fundamental influences on the simulation and prediction of the ISM,
489 the skill of WRF-gray in simulating the MISO is quantitatively assessed in this study. The NLSA
490 MISO indices developed by Sabeerali et al. (2017) are applied in this study to construct the



491 MISO phase composites of surface rainfall and atmospheric circulations from WRF-gray and
492 observations. The enhanced rainfall anomalies show a clear northeastward propagation from the
493 MISO Phases 1 to 8. WRF-gray well captures this northeastward propagation and also simulates
494 the spatial distribution of rainfall anomalies during different phases of the MISO. The low-level
495 westerly wind over the Arabian Sea and Somali jet are strengthened (weakened) during the
496 active (break) phase of the MISO, which induces higher (lower) precipitable water and stronger
497 (weaker) precipitation over the Indian subcontinent. These features can also be well reproduced
498 in WRF-gray, though the amplitude of rainfall, precipitable water and wind anomalies in
499 WRF-gray are larger than that in observations. When compared with WRF-27km, the systematic
500 biases in simulating the MISO have been reduced considerably in WRF-gray, which shows that
501 the cloud-permitting RCM is able to improve the simulations of the MISO associated with the
502 ISM.

503 While WRF-gray captures many aspects of the ISM and MISO qualitatively, quantitative
504 model biases are still apparent. These biases may be induced by various reasons such as the
505 initial conditions. More comprehensive investigation of the predictability of the ISO and MISO
506 in RCM at gray zone resolution is deserved future studies.

507

508

509

510 **Acknowledgements:** Many thanks to Ajaya Ravindran and Sabeerali Cherumadanakadan
511 Thelliyil for the multiple discussions that led to this paper. The author Xingchao Chen and
512 Olivier Pauluis are supported by the New York University in Abu Dhabi Research Institute under
513 grant G1102. The computations were carried out on the High Performance Computing resources



514 at NYUAD. TRMM precipitation data were obtained from the NASA Goddard Space Flight
515 Center. ECMWF reanalysis data were retrieved from the ECMWF Public Datasets web interface
516 (<http://apps.ecmwf.int/datasets/>). WRF output can be made accessible by contacting
517 xzc55@psu.edu.

518



519

520

REFERENCES

521

- 522 Ajayamohan, R. S., and Goswami, B. N.: Potential predictability of the Asian summer monsoon on monthly and
523 seasonal time scales, *Meteorology and Atmospheric Physics*, 84, 83-100, 10.1007/s00703-002-0576-4, 2003.
- 524 Ajayamohan, R. S.: Simulation of South-Asian Summer Monsoon in a GCM, *Pure and Applied Geophysics*, 164,
525 2117-2140, 10.1007/s00024-007-0249-9, 2007.
- 526 Ajayamohan, R. S., Khouider, B., and Majda, A. J.: Simulation of monsoon intraseasonal oscillations in a
527 coarse-resolution aquaplanet GCM, *Geophys. Res. Lett.*, 41, 5662-5669, 10.1002/2014GL060662, 2014.
- 528 Betts, A. K., and Miller, M. J.: A new convective adjustment scheme. Part II: Single column tests using GATE wave,
529 BOMEX, ATEX and arctic air-mass data sets, *Q. J. R. Meteorol. Soc.*, 112, 693-709, 10.1002/qj.49711247308, 1986.
- 530 Bhaskaran, B., Mitchell, J. F. B., Lavery, J. R., and Lal, M.: Climatic response of the Indian subcontinent to doubled
531 CO₂ concentrations, *Int. J. Climatol.*, 15, 873-892, 10.1002/joc.3370150804, 1995.
- 532 Bhaskaran, B., Jones, R. G., Murphy, J. M., and Noguer, M.: Simulations of the Indian summer monsoon using a
533 nested regional climate model: domain size experiments, *Climate Dynam.*, 12, 573-587, 10.1007/bf00216267,
534 1996.
- 535 Bhaskaran, B., Murphy, J. M., and Jones, R. G.: Intraseasonal Oscillation in the Indian Summer Monsoon Simulated
536 by Global and Nested Regional Climate Models, *Mon. Wea. Rev.*, 126, 3124-3134,
537 10.1175/1520-0493(1998)126<3124:ioitis>2.0.co;2, 1998.
- 538 Bollasina, M. A.: Hydrology: Probing the monsoon pulse, *Nature Clim. Change*, 4, 422-423, 10.1038/nclimate2243,
539 2014.
- 540 Bryan, G. H., Wyngaard, J. C., and Fritsch, J. M.: Resolution Requirements for the Simulation of Deep Moist
541 Convection, *Mon. Wea. Rev.*, 131, 2394-2416, 10.1175/1520-0493(2003)131<2394:rrftso>2.0.co;2, 2003.
- 542 Chatterjee, P., and Goswami, B. N.: Structure, genesis and scale selection of the tropical quasi-biweekly mode, *Q. J. R. Meteorol. Soc.*, 130, 1171-1194, 10.1256/qj.03.133, 2004.
- 544 Chen, F., and Dudhia, J.: Coupling an Advanced Land Surface-Hydrology Model with the Penn State-NCAR MMS
545 Modeling System. Part I: Model Implementation and Sensitivity, *Mon. Wea. Rev.*, 129, 569-585,
546 10.1175/1520-0493(2001)129<0569:caalsh>2.0.co;2, 2001.
- 547 Chen, G.-S., Liu, Z., Clemens, S. C., Prell, W. L., and Liu, X.: Modeling the time-dependent response of the Asian
548 summer monsoon to obliquity forcing in a coupled GCM: a PHASEMAP sensitivity experiment, *Climate Dynam.*, 36,
549 695-710, 10.1007/s00382-010-0740-3, 2011.
- 550 Das, S., Mitra, A. K., Iyengar, G. R., and Mohandas, S.: Comprehensive test of different cumulus parameterization
551 schemes for the simulation of the Indian summer monsoon, *Meteorology and Atmospheric Physics*, 78, 227-244,
552 10.1007/s703-001-8176-1, 2001.
- 553 Dash, S. K., Shekhar, M. S., and Singh, G. P.: Simulation of Indian summer monsoon circulation and rainfall using
554 RegCM3, *Theoretical and Applied Climatology*, 86, 161-172, 10.1007/s00704-006-0204-1, 2006.
- 555 Dee, D. P., Uppala, S. M., Simmons, A. J., Berrisford, P., Poli, P., Kobayashi, S., Andrae, U., Balsameda, M. A., Balsamo,
556 G., Bauer, P., Bechtold, P., Beljaars, A. C. M., van de Berg, L., Bidlot, J., Bormann, N., Delsol, C., Dragani, R., Fuentes,
557 M., Geer, A. J., Haimberger, L., Healy, S. B., Hersbach, H., Hólm, E. V., Isaksen, L., Kållberg, P., Köhler, M., Matricardi,
558 M., McNally, A. P., Monge-Sanz, B. M., Morcrette, J. J., Park, B. K., Peubey, C., de Rosnay, P., Tavalato, C., Thépaut, J.
559 N., and Vitart, F.: The ERA-Interim reanalysis: configuration and performance of the data assimilation system, *Q. J. R. Meteorol. Soc.*, 137, 553-597, 10.1002/qj.828, 2011.
- 561 Giannakis, D., and Majda, A. J.: Comparing low-frequency and intermittent variability in comprehensive climate
562 models through nonlinear Laplacian spectral analysis, *Geophys. Res. Lett.*, 39, 10.1029/2012GL051575, 2012a.
- 563 Giannakis, D., and Majda, A. J.: Nonlinear Laplacian spectral analysis for time series with intermittency and
564 low-frequency variability, *Proceedings of the National Academy of Sciences*, 109, 2222-2227,
565 10.1073/pnas.1118984109, 2012b.
- 566 Giorgi, F.: Regional climate modeling: Status and perspectives, *J. Phys. IV France*, 139, 101-118, 2006.
- 567 Goswami, B.: Dynamical predictability of seasonal monsoon rainfall: Problems and prospects,
568 PROCEEDINGS-INDIAN NATIONAL SCIENCE ACADEMY PART A, 60, 101-101, 1994.
- 569 Goswami, B. B., and Goswami, B. N.: A road map for improving dry-bias in simulating the South Asian monsoon
570 precipitation by climate models, *Climate Dynam.*, 1-10, 10.1007/s00382-016-3439-2, 2016.



- 571 Goswami, B. N., and Ajayamohan, R. S.: Intraseasonal Oscillations and Interannual Variability of the Indian Summer
572 Monsoon, *J. Climate*, 14, 1180-1198, [10.1175/1520-0442\(2001\)014<1180:ioaivo>2.0.co;2](https://doi.org/10.1175/1520-0442(2001)014<1180:ioaivo>2.0.co;2), 2001.
- 573 Goswami, B. N., Ajayamohan, R. S., Xavier, P. K., and Sengupta, D.: Clustering of synoptic activity by Indian summer
574 monsoon intraseasonal oscillations, *Geophys. Res. Lett.*, 30, [10.1029/2002GL016734](https://doi.org/10.1029/2002GL016734), 2003.
- 575 Grell, G. A., and Dévényi, D.: A generalized approach to parameterizing convection combining ensemble and data
576 assimilation techniques, *Geophys. Res. Lett.*, 29, 38-31-38-34, [10.1029/2002GL015311](https://doi.org/10.1029/2002GL015311), 2002.
- 577 Hong, S.-Y., Noh, Y., and Dudhia, J.: A New Vertical Diffusion Package with an Explicit Treatment of Entrainment
578 Processes, *Mon. Wea. Rev.*, 134, 2318-2341, [10.1175/mwr3199.1](https://doi.org/10.1175/mwr3199.1), 2006.
- 579 Hu, X.-M., Nielsen-Gammon, J. W., and Zhang, F.: Evaluation of Three Planetary Boundary Layer Schemes in the
580 WRF Model, *J. Appl. Meteor. Climatol.*, 49, 1831-1844, [10.1175/2010jamc2432.1](https://doi.org/10.1175/2010jamc2432.1), 2010.
- 581 Huffman, G. J., Adler, R. F., Morrissey, M. M., Bolvin, D. T., Curtis, S., Joyce, R., McGavock, B., and Susskind, J.: Global
582 Precipitation at One-Degree Daily Resolution from Multisatellite Observations, *Journal of Hydrometeorology*, 2,
583 36-50, [10.1175/1525-7541\(2001\)002<0036:gpaodd>2.0.co;2](https://doi.org/10.1175/1525-7541(2001)002<0036:gpaodd>2.0.co;2), 2001.
- 584 Iacono, M. J., Delamere, J. S., Mlawer, E. J., Shephard, M. W., Clough, S. A., and Collins, W. D.: Radiative forcing by
585 long-lived greenhouse gases: Calculations with the AER radiative transfer models, *J. Geophys. Res. Atmos.*, 113,
586 [10.1029/2008JD009944](https://doi.org/10.1029/2008JD009944), 2008.
- 587 Jain, S. K., and Kumar, V.: Trend analysis of rainfall and temperature data for India, *Current Science(Bangalore)*, 102,
588 37-49, 2012.
- 589 Janjić, Z. I.: The Step-Mountain Eta Coordinate Model: Further Developments of the Convection, Viscous Sublayer,
590 and Turbulence Closure Schemes, *Mon. Wea. Rev.*, 122, 927-945,
591 [10.1175/1520-0493\(1994\)122<0927:tsmecn>2.0.co;2](https://doi.org/10.1175/1520-0493(1994)122<0927:tsmecn>2.0.co;2), 1994.
- 592 Ji, Y., and Vernekar, A. D.: Simulation of the Asian Summer Monsoons of 1987 and 1988 with a Regional Model
593 Nested in a Global GCM, *J. Climate*, 10, 1965-1979, [10.1175/1520-0442\(1997\)010<1965:sotasm>2.0.co;2](https://doi.org/10.1175/1520-0442(1997)010<1965:sotasm>2.0.co;2), 1997.
- 594 Jiang, X., Li, T., and Wang, B.: Structures and Mechanisms of the Northward Propagating Boreal Summer
595 Intraseasonal Oscillation, *J. Climate*, 17, 1022-1039, [10.1175/1520-0442\(2004\)017<1022:samotn>2.0.co;2](https://doi.org/10.1175/1520-0442(2004)017<1022:samotn>2.0.co;2), 2004.
- 596 Joseph, P. V., and Sijikumar, S.: Intraseasonal Variability of the Low-Level Jet Stream of the Asian Summer Monsoon,
597 *J. Climate*, 17, 1449-1458, [10.1175/1520-0442\(2004\)017<1449:ivotlj>2.0.co;2](https://doi.org/10.1175/1520-0442(2004)017<1449:ivotlj>2.0.co;2), 2004.
- 598 Kain, J. S.: The Kain-Fritsch Convective Parameterization: An Update, *J. Appl. Meteorol.*, 43, 170-181,
599 [10.1175/1520-0450\(2004\)043<0170:tkcpau>2.0.co;2](https://doi.org/10.1175/1520-0450(2004)043<0170:tkcpau>2.0.co;2), 2004.
- 600 Kikuchi, K., Wang, B., and Kajikawa, Y.: Bimodal representation of the tropical intraseasonal oscillation, *Climate*
601 *Dynam.*, 38, 1989-2000, [10.1007/s00382-011-1159-1](https://doi.org/10.1007/s00382-011-1159-1), 2012.
- 602 Klemp, J. B., Dudhia, J., and Hassiotis, A. D.: An Upper Gravity-Wave Absorbing Layer for NWP Applications, *Mon.*
603 *Wea. Rev.*, 136, 3987-4004, [10.1175/2008mwr2596.1](https://doi.org/10.1175/2008mwr2596.1), 2008.
- 604 Kolusu, S., Prasanna, V., and Preethi, B.: Simulation of Indian summer monsoon intra-seasonal oscillations using
605 WRF regional atmospheric model, *International Journal of Earth and Atmospheric Science*, 1, 35-53, 2014.
- 606 Krishnamurthy, V., and Shukla, J.: Intraseasonal and Seasonally Persisting Patterns of Indian Monsoon Rainfall, *J.*
607 *Climate*, 20, 3-20, [10.1175/jcli3981.1](https://doi.org/10.1175/jcli3981.1), 2007.
- 608 Krishnamurti, T. N., and Bhalme, H. N.: Oscillations of a Monsoon System. Part I. Observational Aspects, *J. Atmos.*
609 *Sci.*, 33, 1937-1954, [10.1175/1520-0469\(1976\)033<1937:ooamp>2.0.co;2](https://doi.org/10.1175/1520-0469(1976)033<1937:ooamp>2.0.co;2), 1976.
- 610 Lau, N.-C., and Ploshay, J. J.: Simulation of Synoptic- and Subsynchronous-Scale Phenomena Associated with the East
611 Asian Summer Monsoon Using a High-Resolution GCM, *Mon. Wea. Rev.*, 137, 137-160, [10.1175/2008mwr2511.1](https://doi.org/10.1175/2008mwr2511.1),
612 2009.
- 613 Lau, W. K.-M., and Waliser, D. E.: Intraseasonal variability in the atmosphere-ocean climate system, *Springer Science*
614 *& Business Media*, 2011.
- 615 Lee, J.-Y., Wang, B., Wheeler, M. C., Fu, X., Waliser, D. E., and Kang, I.-S.: Real-time multivariate indices for the
616 boreal summer intraseasonal oscillation over the Asian summer monsoon region, *Climate Dynam.*, 40, 493-509,
617 [10.1007/s00382-012-1544-4](https://doi.org/10.1007/s00382-012-1544-4), 2013.
- 618 Lim, K.-S. S., and Hong, S.-Y.: Development of an Effective Double-Moment Cloud Microphysics Scheme with
619 Prognostic Cloud Condensation Nuclei (CCN) for Weather and Climate Models, *Mon. Wea. Rev.*, 138, 1587-1612,
620 [10.1175/2009mwr2968.1](https://doi.org/10.1175/2009mwr2968.1), 2010.
- 621 Lucas-Picher, P., Christensen, J. H., Saeed, F., Kumar, P., Asharaf, S., Ahrens, B., Wiltshire, A. J., Jacob, D., and
622 Hagemann, S.: Can regional climate models represent the Indian monsoon?, *Journal of Hydrometeorology*, 12,
623 849-868, 2011.



- 624 Madden, R. A., and Julian, P. R.: Detection of a 40–50 Day Oscillation in the Zonal Wind in the Tropical Pacific, *J.*
625 *Atmos. Sci.*, 28, 702-708, [10.1175/1520-0469\(1971\)028<0702:doadoi>2.0.co;2](https://doi.org/10.1175/1520-0469(1971)028<0702:doadoi>2.0.co;2), 1971.
- 626 Mukhopadhyay, P., Taraphdar, S., Goswami, B., and Krishnakumar, K.: Indian summer monsoon precipitation
627 climatology in a high-resolution regional climate model: Impacts of convective parameterization on systematic
628 biases, *Wea. Forecasting*, 25, 369-387, 2010.
- 629 Najar, K. A. A., and Salvekar, P. S.: Understanding the Tropical Cyclone Gonu, in: Indian Ocean Tropical Cyclones and
630 Climate Change, edited by: Charabi, Y., Springer Netherlands, Dordrecht, 359-369, 2010.
- 631 Oouchi, K., Noda, A. T., Satoh, M., Wang, B., Xie, S.-P., Takahashi, H. G., and Yasunari, T.: Asian summer monsoon
632 simulated by a global cloud-system-resolving model: Diurnal to intra-seasonal variability, *Geophys. Res. Lett.*, 36,
633 [10.1029/2009GL038271](https://doi.org/10.1029/2009GL038271), 2009.
- 634 Pauluis, O., and Garner, S.: Sensitivity of Radiative–Convective Equilibrium Simulations to Horizontal Resolution, *J.*
635 *Atmos. Sci.*, 63, 1910-1923, [10.1175/jas3705.1](https://doi.org/10.1175/jas3705.1), 2006.
- 636 Pleim, J. E.: A Combined Local and Nonlocal Closure Model for the Atmospheric Boundary Layer. Part I: Model
637 Description and Testing, *J. Appl. Meteor. Climatol.*, 46, 1383-1395, [10.1175/jam2539.1](https://doi.org/10.1175/jam2539.1), 2007.
- 638 Prein, A. F., Langhans, W., Fosser, G., Ferrone, A., Ban, N., Goergen, K., Tölle, M., Gutjahr, O., Feser, F.,
639 Brisson, E., Kollet, S., Schmidli, J., van Lipzig, N. P. M., and Leung, R.: A review on regional convection-permitting
640 climate modeling: Demonstrations, prospects, and challenges, *Rev. Geophys.*, 53, 323-361, [10.1002/2014RG000475](https://doi.org/10.1002/2014RG000475),
641 2015.
- 642 Rajendran, K., and Kitoh, A.: Indian summer monsoon in future climate projection by a super high-resolution global
643 model, *Current Science (00113891)*, 95, 1560-1569, 2008.
- 644 Raju, A., Parekh, A., Chowdary, J. S., and Gnanaseelan, C.: Assessment of the Indian summer monsoon in the WRF
645 regional climate model, *Climate Dynam.*, 44, 3077-3100, [10.1007/s00382-014-2295-1](https://doi.org/10.1007/s00382-014-2295-1), 2015.
- 646 Ramu, D. A., Sabeerali, C. T., Chattopadhyay, R., Rao, D. N., George, G., Dhakate, A. R., Salunke, K., Srivastava, A.,
647 and Rao, S. A.: Indian summer monsoon rainfall simulation and prediction skill in the CFSv2 coupled model: Impact
648 of atmospheric horizontal resolution, *J. Geophys. Res. Atmos.*, 121, 2205-2221, [10.1002/2015JD024629](https://doi.org/10.1002/2015JD024629), 2016.
- 649 Ratnam, J. V., and Kumar, K. K.: Sensitivity of the Simulated Monsoons of 1987 and 1988 to Convective
650 Parameterization Schemes in MM5, *J. Climate*, 18, 2724-2743, [10.1175/jcli3390.1](https://doi.org/10.1175/jcli3390.1), 2005.
- 651 Rockel, B., and Geyer, B.: The performance of the regional climate model CLM in different climate regions, based on
652 the example of precipitation, *Meteorologische Zeitschrift*, 17, 487-498, 2008.
- 653 Sabeerali, C. T., Rao, S. A., Ajayamohan, R. S., and Murtugudde, R.: On the relationship between Indian summer
654 monsoon withdrawal and Indo-Pacific SST anomalies before and after 1976/1977 climate shift, *Climate Dynam.*, 39,
655 841-859, [10.1007/s00382-011-1269-9](https://doi.org/10.1007/s00382-011-1269-9), 2012.
- 656 Sabeerali, C. T., Ajayamohan, R. S., Giannakis, D., and Majda, A. J.: Extraction and prediction of indices for monsoon
657 intraseasonal oscillations: an approach based on nonlinear Laplacian spectral analysis, *Climate Dynam.*, 1-20,
658 [10.1007/s00382-016-3491-y](https://doi.org/10.1007/s00382-016-3491-y), 2017.
- 659 Saeed, F., Hagemann, S., and Jacob, D.: A framework for the evaluation of the South Asian summer monsoon in a
660 regional climate model applied to REMO, *Int. J. Climatol.*, 32, 430-440, [10.1002/joc.2285](https://doi.org/10.1002/joc.2285), 2012.
- 661 Samala, B. K., C. N., Banerjee, S., Kaginalkar, A., and Dalvi, M.: Study of the Indian summer monsoon using WRF–
662 ROMS regional coupled model simulations, *Atmospheric Science Letters*, 14, 20-27, [10.1002/asl2.409](https://doi.org/10.1002/asl2.409), 2013.
- 663 Shi, J. J., Tao, W.-K., Matsui, T., Cifelli, R., Hou, A., Lang, S., Tokay, A., Wang, N.-Y., Peters-Lidard, C.,
664 Skofronick-Jackson, G., Rutledge, S., and Petersen, W.: WRF Simulations of the 20–22 January 2007 Snow Events
665 over Eastern Canada: Comparison with In Situ and Satellite Observations, *J. Appl. Meteor. Climatol.*, 49, 2246-2266,
666 [10.1175/2010jamc2282.1](https://doi.org/10.1175/2010jamc2282.1), 2010.
- 667 Sikka, D. R., and Gadgil, S.: On the Maximum Cloud Zone and the ITCZ over Indian, Longitudes during the Southwest
668 Monsoon, *Mon. Wea. Rev.*, 108, 1840-1853, [10.1175/1520-0493\(1980\)108<1840:OTMCZA>2.0.CO;2](https://doi.org/10.1175/1520-0493(1980)108<1840:OTMCZA>2.0.CO;2), 1980.
- 669 Skamarock, W., Klemp, J., Dudhia, J., Gill, D., Barker, D., Duda, M., Huang, X., Wang, W., and Powers, J.: A
670 Description of the Advanced Research WRF Version 3 (2008) NCAR Technical Note, Boulder, CO, 2008.
- 671 Srinivas, C. V., Hariprasad, D., Bhaskar Rao, D. V., Anjaneyulu, Y., Baskaran, R., and Venkatraman, B.: Simulation of
672 the Indian summer monsoon regional climate using advanced research WRF model, *Int. J. Climatol.*, 33, 1195-1210,
673 [10.1002/joc.3505](https://doi.org/10.1002/joc.3505), 2013.
- 674 Suhas, E., Neena, J. M., and Goswami, B. N.: An Indian monsoon intraseasonal oscillations (MISO) index for real
675 time monitoring and forecast verification, *Climate Dynam.*, 40, 2605-2616, [10.1007/s00382-012-1462-5](https://doi.org/10.1007/s00382-012-1462-5), 2013.
- 676 Vernekar, A. D., and Ji, Y.: Simulation of the Onset and Intraseasonal Variability of Two Contrasting Summer



- 677 Monsoons, *J. Climate*, 12, 1707-1725, 10.1175/1520-0442(1999)012<1707:sotoai>2.0.co;2, 1999.
- 678 Wang, S., Sobel, A. H., Zhang, F., Sun, Y. Q., Yue, Y., and Zhou, L.: Regional Simulation of the October and November
- 679 MJO Events Observed during the CINDY/DYNAMO Field Campaign at Gray Zone Resolution, *J. Climate*, 28,
- 680 2097-2119, 10.1175/jcli-d-14-00294.1, 2015.
- 681 Yasunari, T.: Structure of an Indian Summer Monsoon System with around 40-Day Period, *Journal of the*
- 682 *Meteorological Society of Japan. Ser. II*, 59, 336-354, 1981.
- 683
- 684



685

Figures

686 Figure 1. Model domain used in the WRF simulations with topography (gray scales) and
687 coastlines (red lines). The black box shows the climatic zone used for the calculation of KELLF
688 index and the blue polygon shows the Indian subcontinent.

689 Figure 2. Averaged daily rainfall over the Indian subcontinent for JJAS in different years from
690 TRMM observation (blue bars), WRF-gray (green bars) and WRF-27km (yellow bars).

691 Figure 3. 5-yr mean monsoon (JJAS) winds (vectors) and geopotential heights (red contours)
692 at 200-hPa from (a) ERA-Interim and (b) WRF-gray; winds (vectors) and precipitable water
693 (color shadings) at 850-hPa from (c) ERA-Interim and (d) WRF-gray; daily surface precipitation
694 (color shadings) from (e) TRMM and (f) WRF-gray. Topography is shown by the black contours
695 starts at 500m with a 1000-m interval.

696 Figure 4. Temporal evolution of KELLF indices in (a) 2007; (b) 2008; (c) 2009; (d) 2010 and
697 (e) 2011 from ERA-Interim (black lines) and WRF-gray (blue lines). A 5-day moving average is
698 applied to the time series.

699 Figure 5. Temporal evolution of daily surface rainfall averaged over the Indian subcontinent in
700 (a) 2007; (b) 2008; (c) 2009; (d) 2010 and (e) 2011 from TRMM (black lines) and WRF-gray
701 (blue lines). A 5-day moving average is applied to the time series.

702 Figure 6. Spatial distributions of averaged daily surface precipitation from May to October in
703 year 2007 derived from (a-f) TRMM and (g-l) WRF-gray.

704 Figure 7. Spatial distributions of averaged daily surface precipitation from May to October in
705 year 2009 derived from (a-f) TRMM and (g-l) WRF-gray.

706 Figure 8. Spatial distributions of averaged daily surface precipitation from May to October in
707 year 2011 derived from (a-f) TRMM and (g-l) WRF-gray.



708 Figure 9. 2D phase space diagrams for the NLSA MISO indices. An anticlockwise
709 propagation from the phase 1 represents MISO's northward propagation. The circle centered at
710 the origin has radius equal to 1.5, which is the threshold for identification of significant MISO
711 events.

712 Figure 10. Phase composites of daily surface rainfall anomalies obtained from TRMM (Figure
713 a-h: phase 1 to 8).

714 Figure 11. Phase composites of daily surface rainfall anomalies obtained from WRF-gray
715 (Figure a-h: phase 1 to 8).

716 Figure 12. Phase composites of daily surface rainfall anomalies obtained from WRF-27km
717 (Figure a-h: phase 1 to 8).

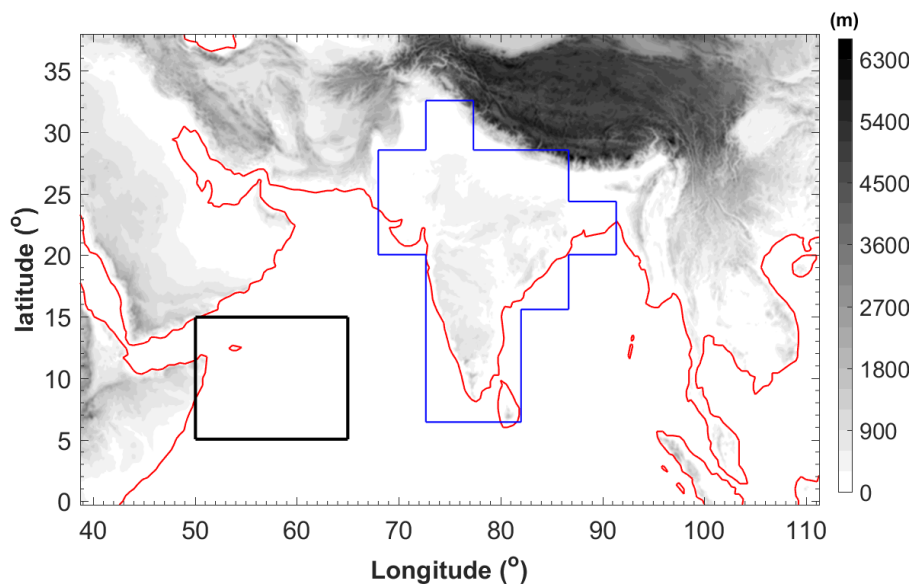
718 Figure 13. Spatial distributions of 10-day averaged daily surface rainfall anomalies in (a, e)
719 1-10 July, (d, f) 11-20 July, (c, g) 21-31 July and (d, h) 01-10 August, 2009 derived from TRMM
720 (left panels) and WRF-gray (right panels).

721 Figure 14. Phase composites of 850-hPa wind and precipitable water anomalies obtained from
722 ERA-Interim (Figure a-h: phase 1 to 8).

723 Figure 15. Phase composites of 850-hPa wind and precipitable water anomalies obtained from
724 WRF-gray (Figure a-h: phase 1 to 8).

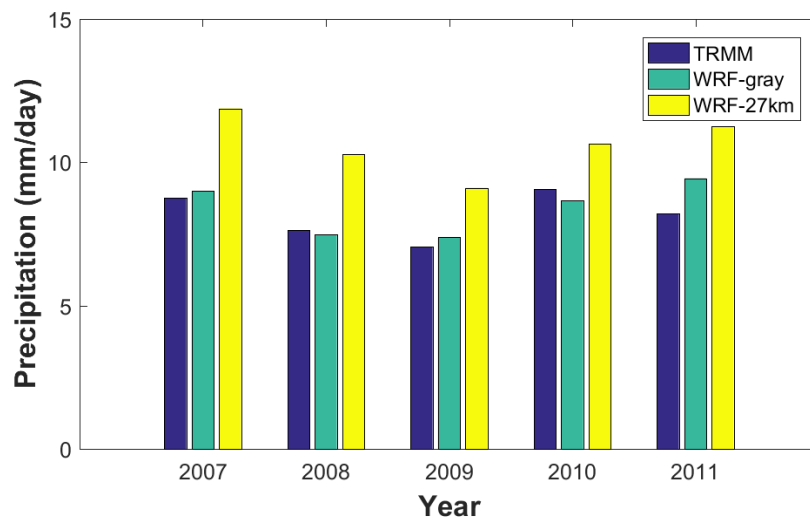
725 Figure 16. Temporal evolutions of (a) KELLF indices, (b) precipitable water averaged over
726 the Indian subcontinent and (c) daily surface precipitation averaged over the Indian subcontinent
727 in year 2007 from ERA-Interim/TRMM (black lines), WRF-gray simulation starts from April 20
728 (blue lines, control run), WRF-gray simulation starts from April 19 (red lines) and WRF-gray
729 simulation starts from April 21 (green lines).

730

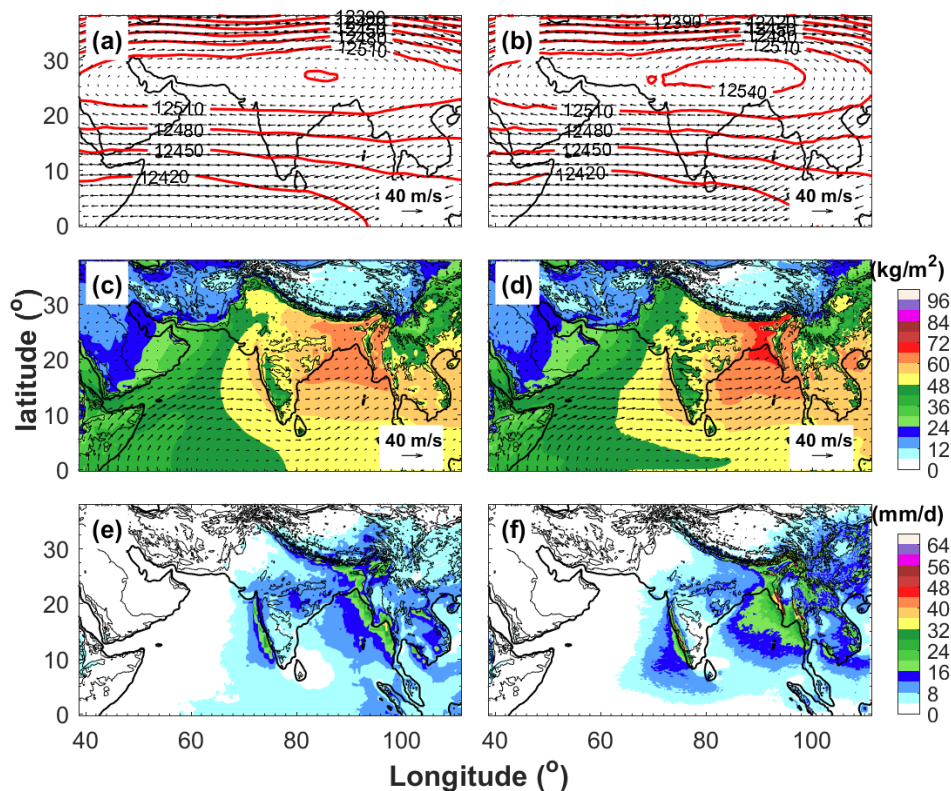


731
732
733
734
735

Figure 1. Model domain used in the WRF simulations with topography (gray scales) and coastlines (red lines). The black box shows the climatic zone used for the calculation of KELLF index and the blue polygon shows the Indian subcontinent.



736
737 Figure 2. Averaged daily rainfall over the Indian subcontinent for JJAS in different years from TRMM
738 observation (blue bars), WRF-gray (green bars) and WRF-27km (yellow bars).
739



740

741

Figure 3. 5-yr mean monsoon (JJAS) winds (vectors) and geopotential heights (red contours) at 200-hPa from

742

(a) ERA-Interim and (b) WRF-gray; winds (vectors) and precipitable water (color shadings) at 850-hPa from (c)

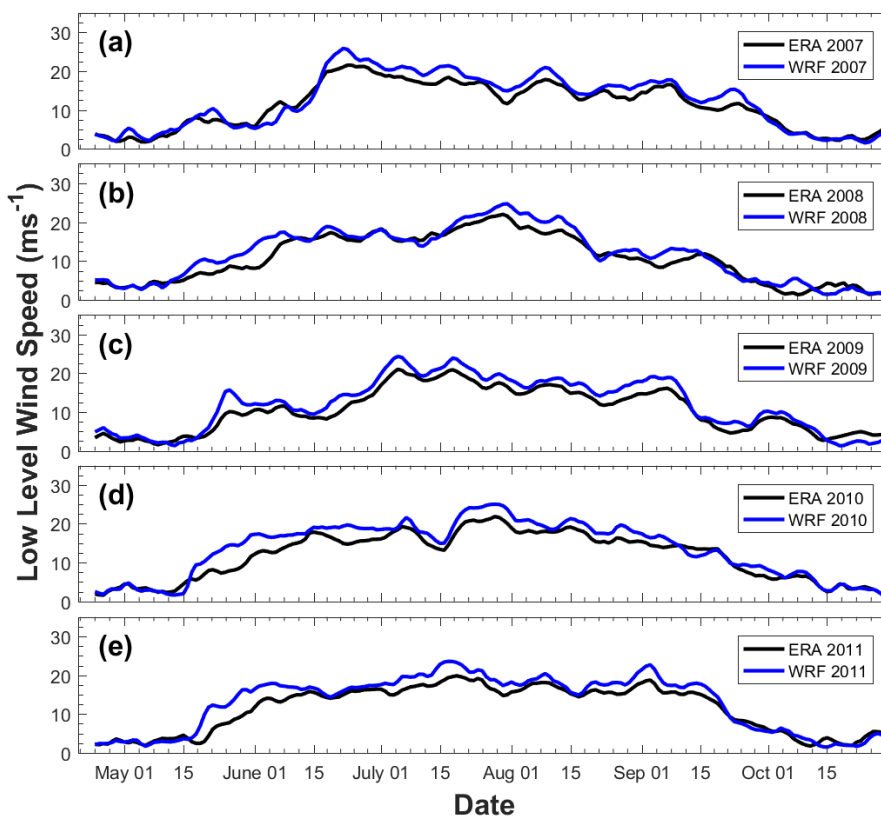
743

ERA-Interim and (d) WRF-gray; daily surface precipitation (color shadings) from (e) TRMM and (f) WRF-gray.

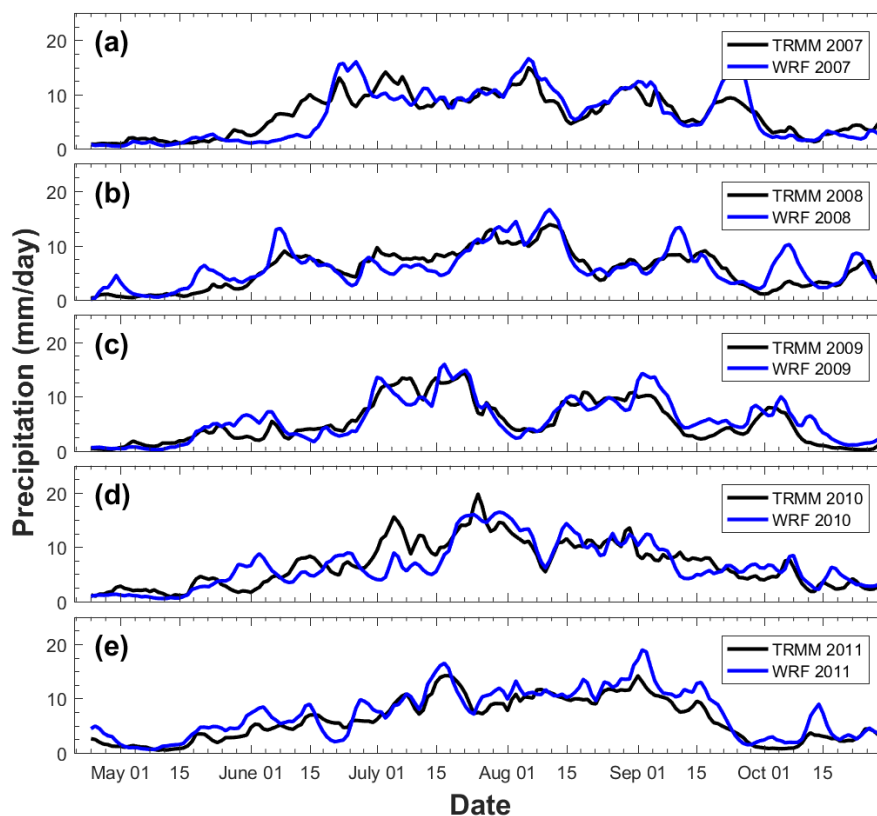
744

Topography is shown by the black contours starts at 500m with a 1000-m interval.

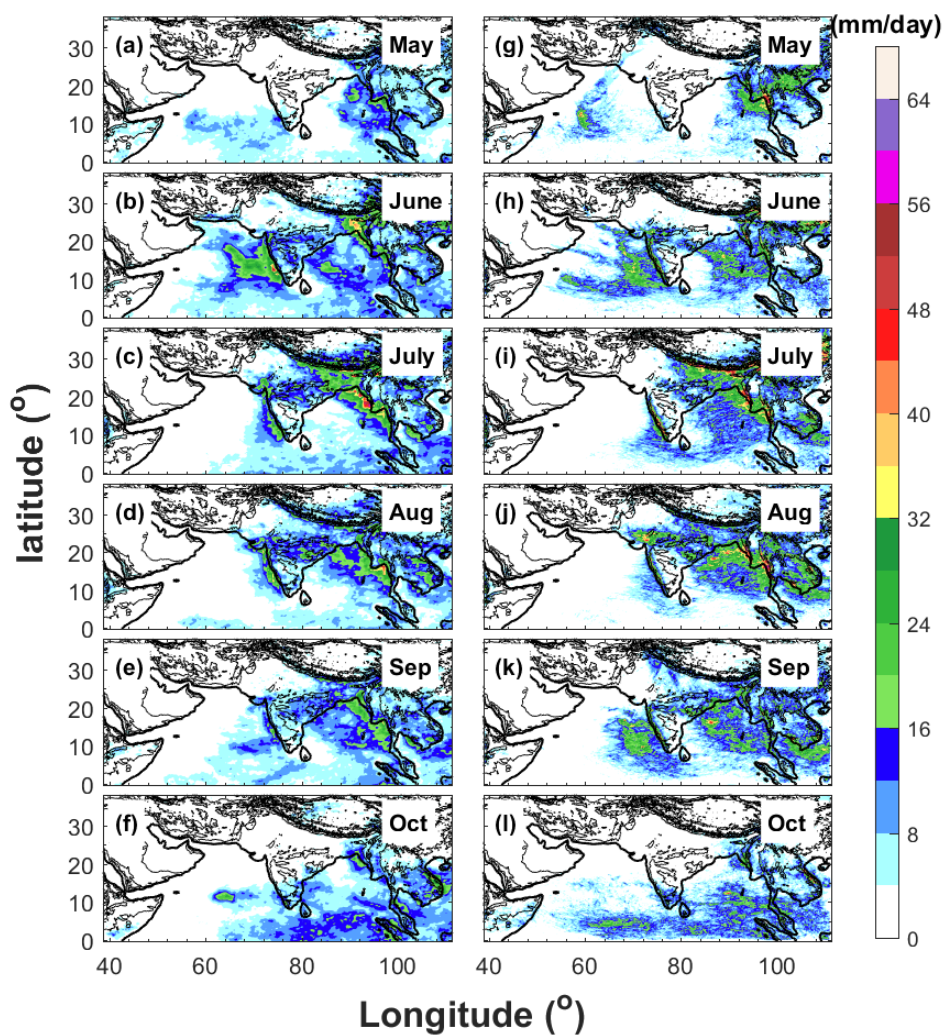
745



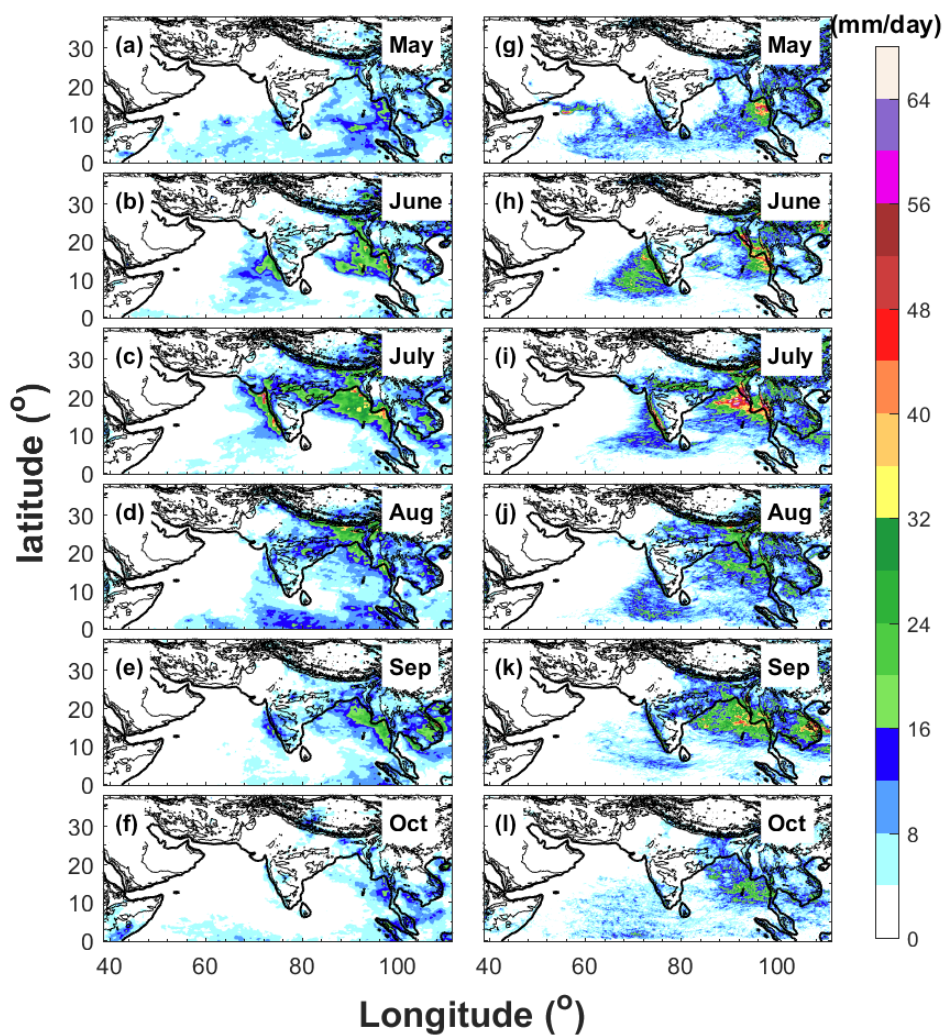
746
747 Figure 4. Temporal evolution of KELLF indices in (a) 2007; (b) 2008; (c) 2009; (d) 2010 and (e) 2011 from
748 ERA-Interim (black lines) and WRF-gray (blue lines). A 5-day moving average is applied to the time series.
749
750



751
752 Figure 5. Temporal evolution of daily surface rainfall averaged over the Indian subcontinent in (a) 2007; (b)
753 2008; (c) 2009; (d) 2010 and (e) 2011 from TRMM (black lines) and WRF-gray (blue lines). A 5-day moving
754 average is applied to the time series.
755

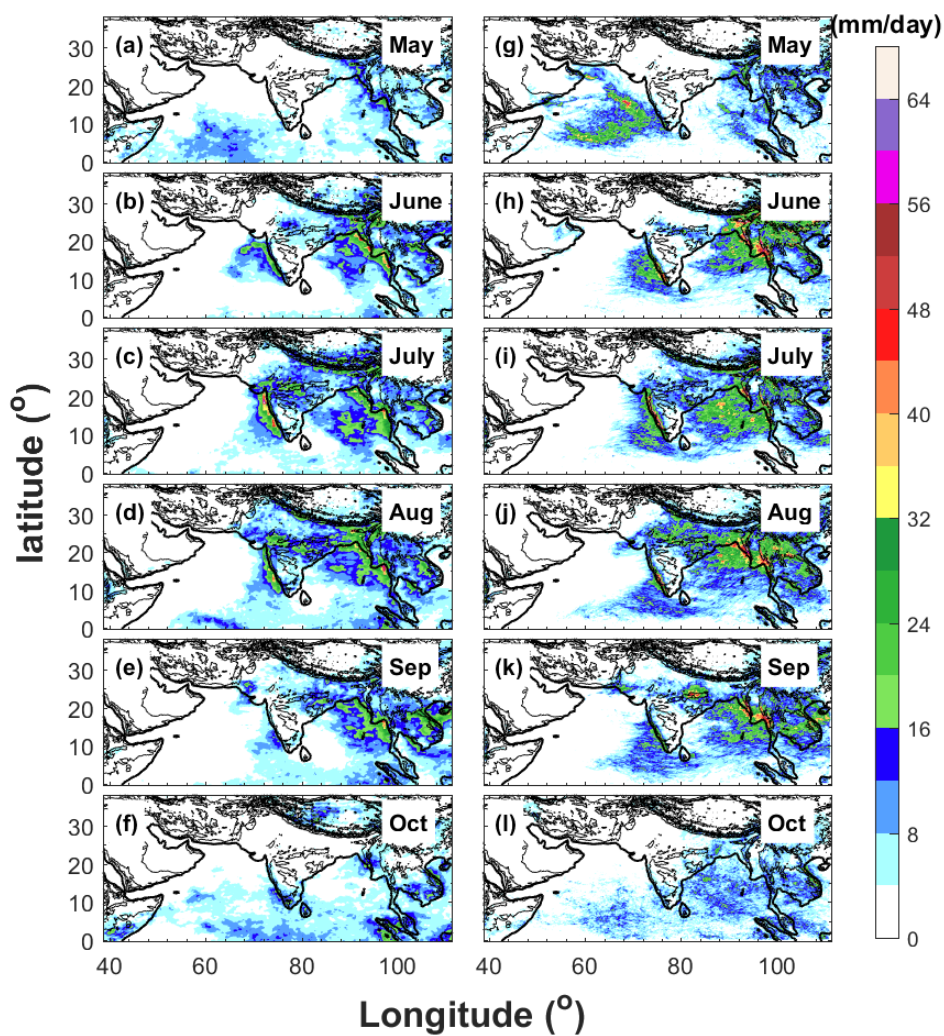


756
757 Figure 6. Spatial distributions of averaged daily surface precipitation from May to October in year 2007
758 derived from (a-f) TRMM and (g-l) WRF-gray.
759

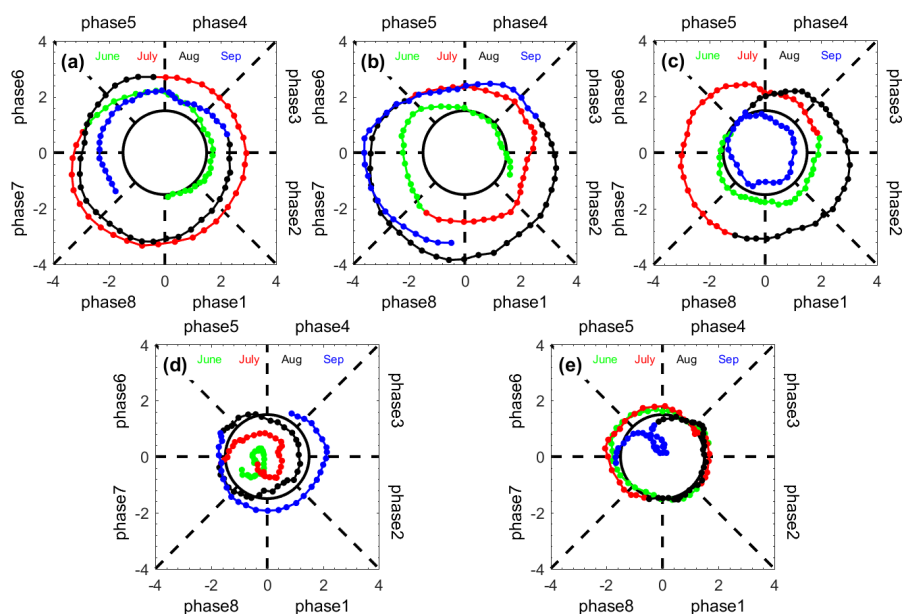


760
761
762
763

Figure 7. Spatial distributions of averaged daily surface precipitation from May to October in year 2009 derived from (a-f) TRMM and (g-l) WRF-gray.



764
765 Figure 8. Spatial distributions of averaged daily surface precipitation from May to October in year 2011
766 derived from (a-f) TRMM and (g-l) WRF-gray.
767



768

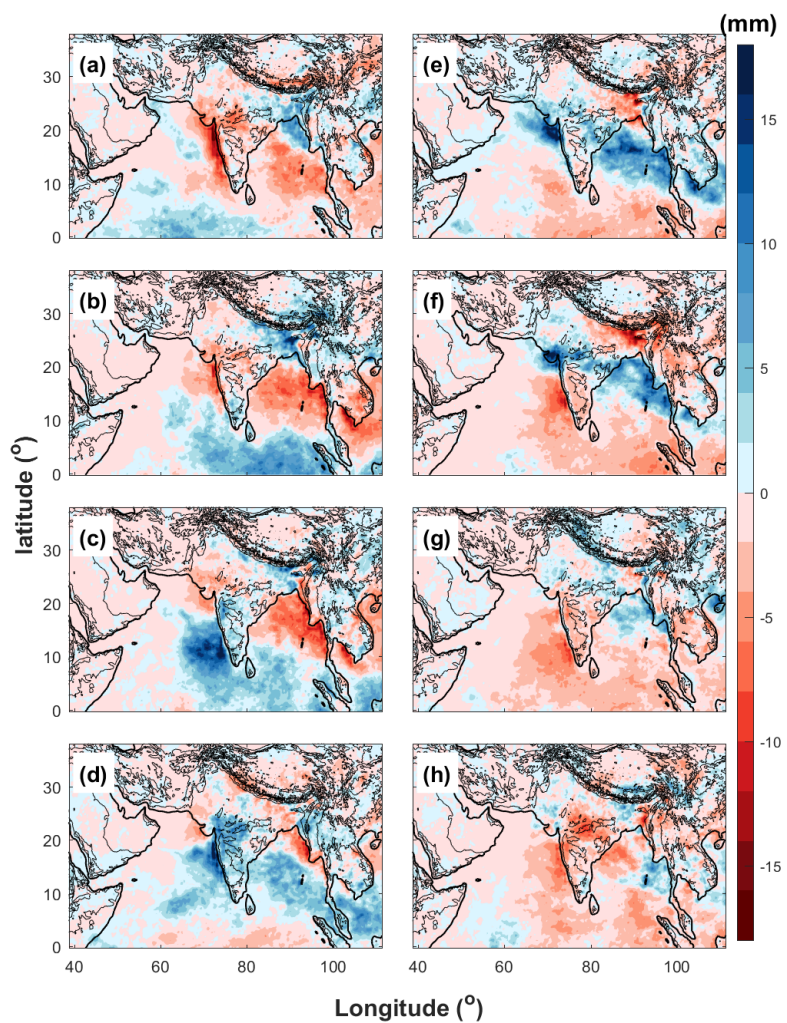
769

770

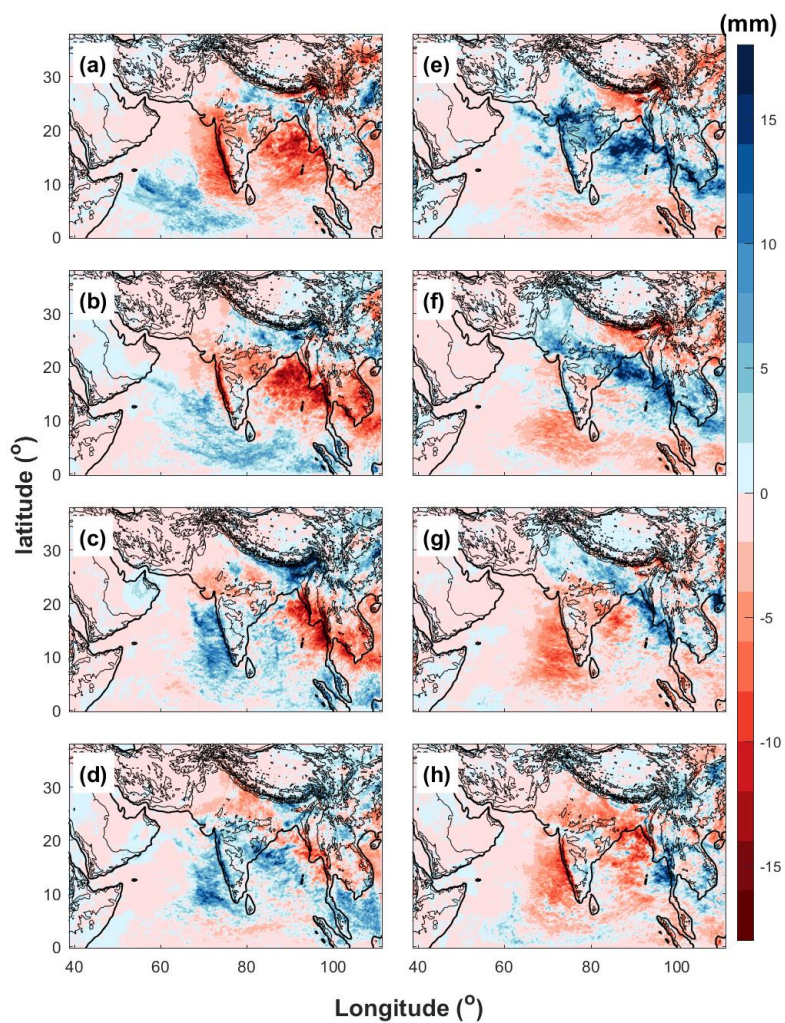
771

772

Figure 9. 2D phase space diagrams for the NLSA MISO indices. An anticlockwise propagation from the phase 1 represents MISO's northward propagation. The circle centered at the origin has radius equal to 1.5, which is the threshold for identification of significant MISO events.

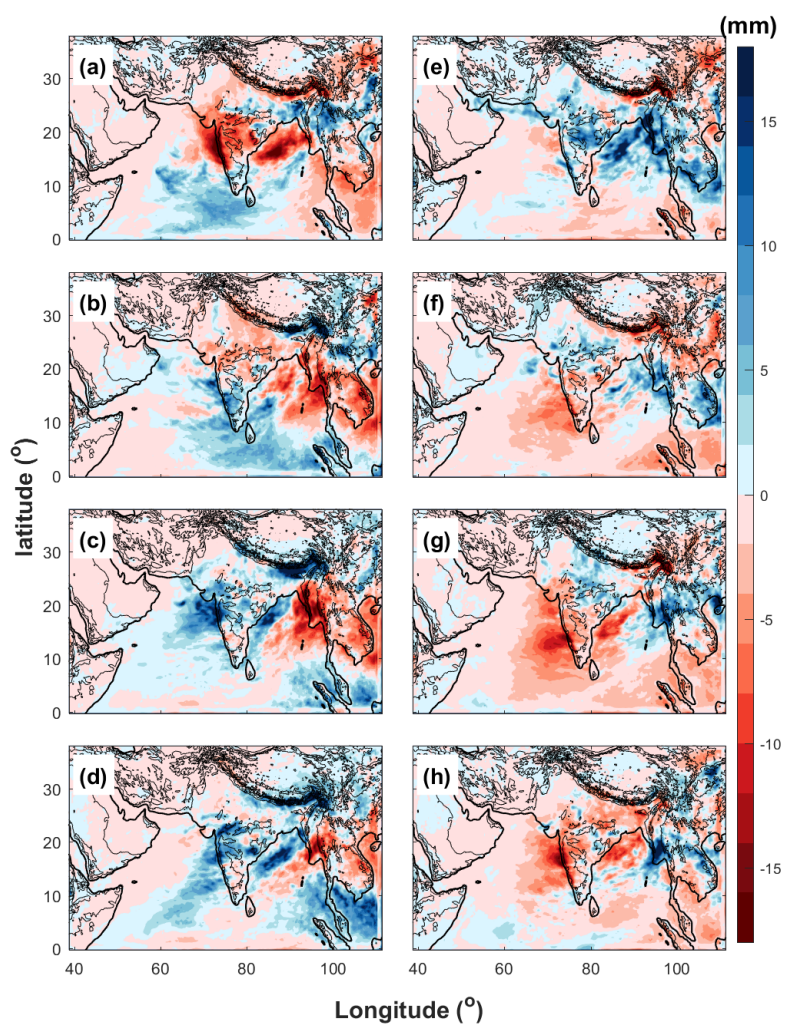


773
774 Figure 10. Phase composites of daily surface rainfall anomalies obtained from TRMM (Figure a-h: phase 1 to
775 8).
776



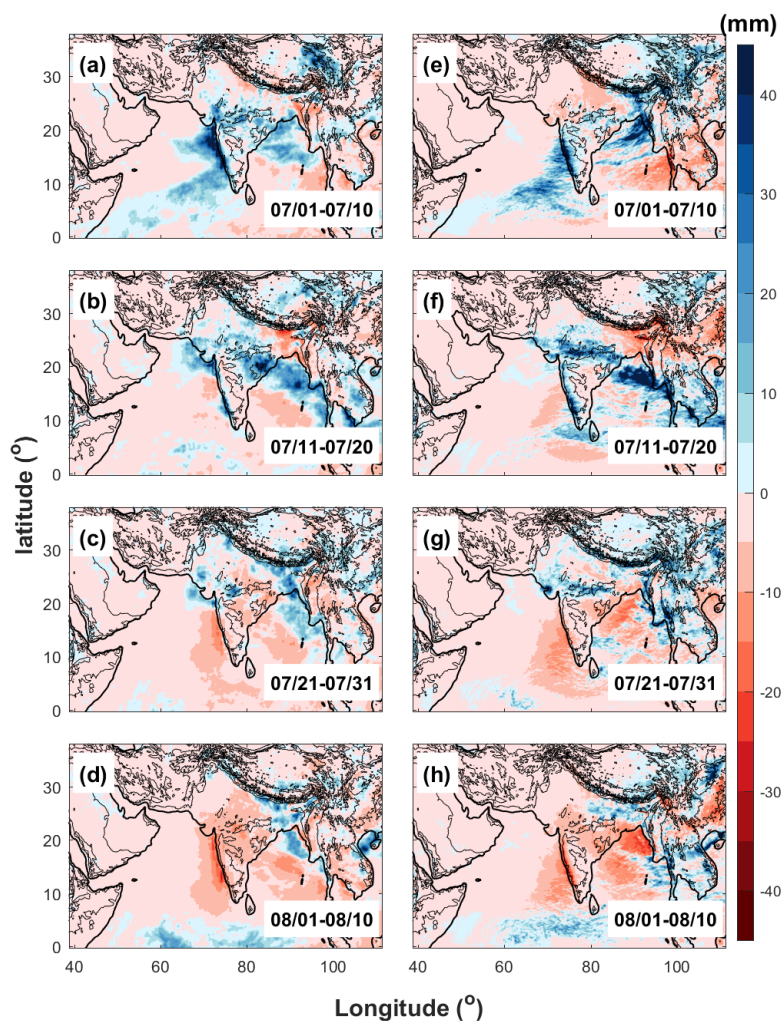
777
778
779
780

Figure 11. Phase composites of daily surface rainfall anomalies obtained from WRF-gray (Figure a-h: phase 1 to 8).



781
782
783
784

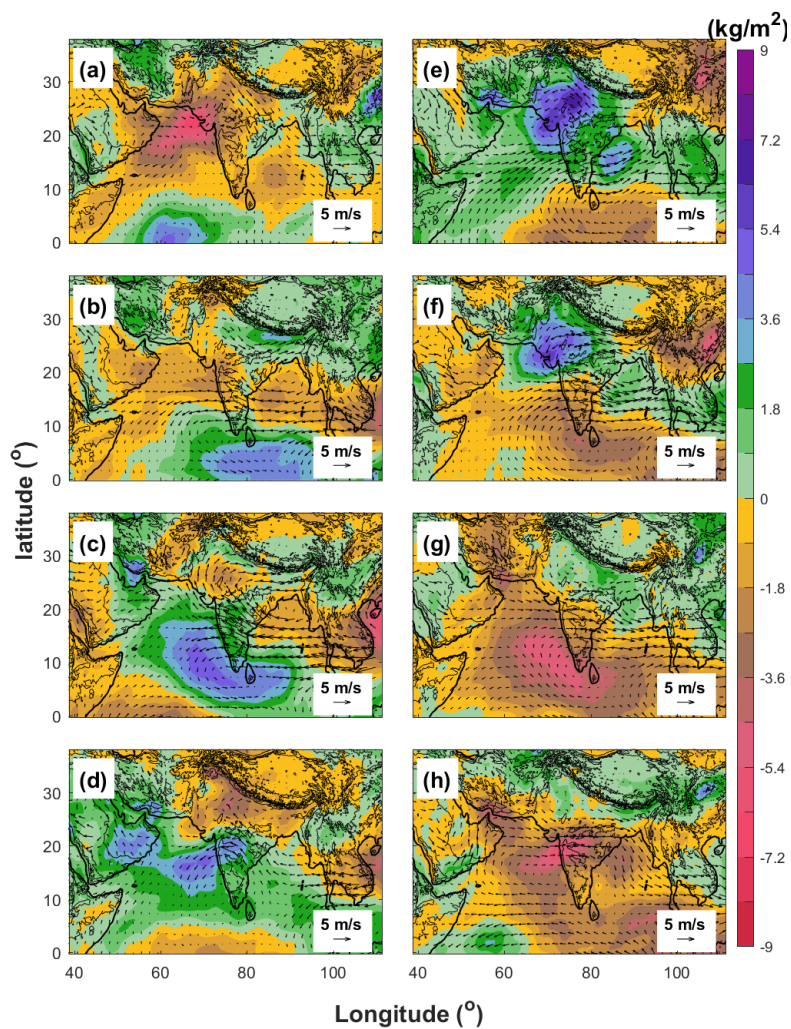
Figure 12. Phase composites of daily surface rainfall anomalies obtained from WRF-27km (Figure a-h: phase 1 to 8).



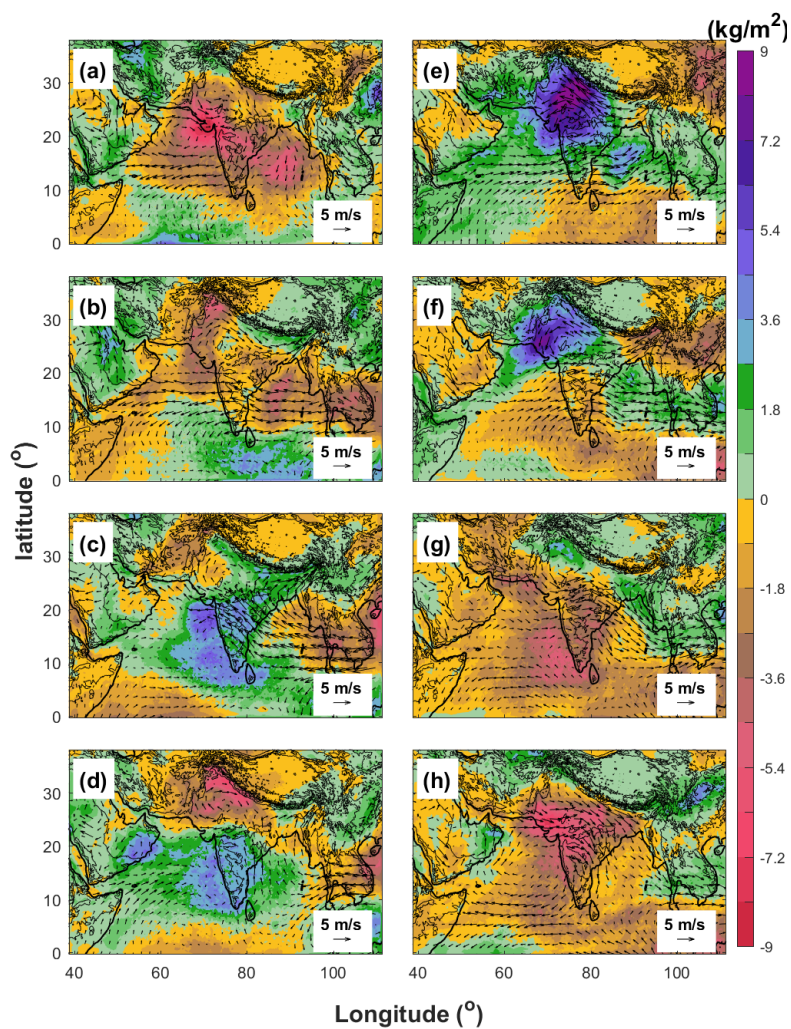
785
786 Figure 13. Spatial distributions of 10-day averaged daily surface rainfall anomalies in (a, e) 1-10 July, (d, f)
787 11-20 July, (c, g) 21-31 July and (d, h) 01-10 August, 2009 derived from TRMM (left panels) and WRF-gray
788 (right panels).
789



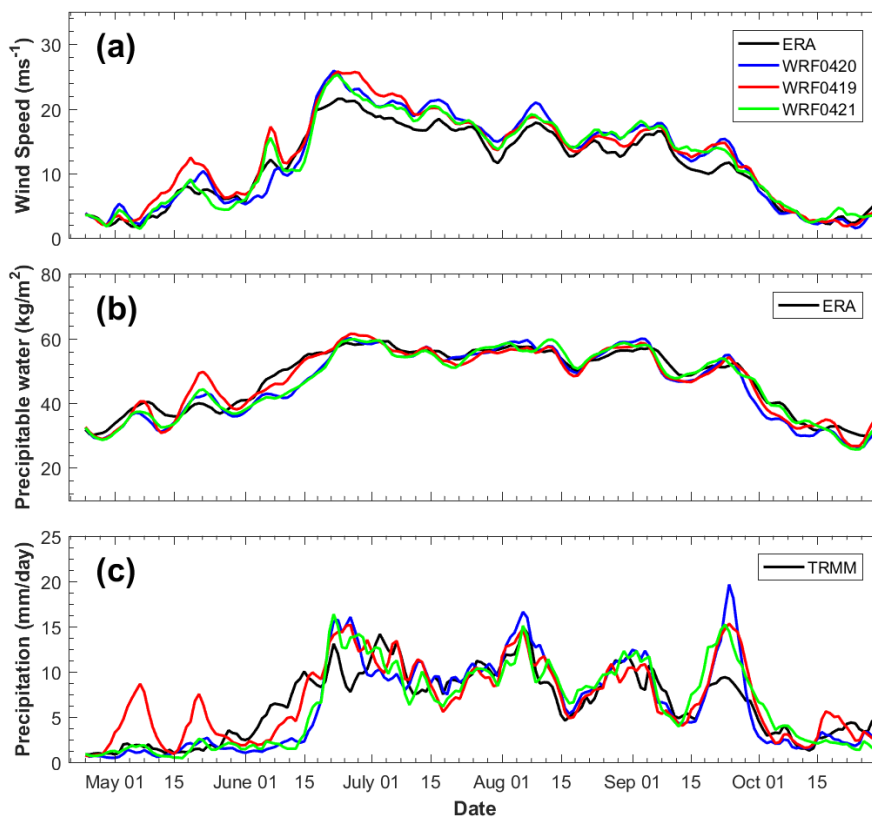
790



791
792 Figure 14. Phase composites of 850-hPa wind and precipitable water anomalies obtained from ERA-Interim
793 (Figure a-h: phase 1 to 8).
794



795
796 Figure 15. Phase composites of 850-hPa wind and precipitable water anomalies obtained from WRF-gray
797 (Figure a-h: phase 1 to 8).
798



799

800 Figure 16. Temporal evolutions of (a) KELLF indices, (b) precipitable water averaged over the Indian

801 subcontinent and (c) daily surface precipitation averaged over the Indian subcontinent in year 2007 from

802 ERA-Interim/TRMM (black lines), WRF-gray simulation starts from April 20 (blue lines, control run), WRF-gray

803 simulation starts from April 19 (red lines) and WRF-gray simulation starts from April 21 (green lines).

804